

Activity report of the Italian CRG beamline at the European Synchrotron Radiation Facility (ESRF)

N. 6 - December 2018

Grenoble, December 2018

©2018 CNR-IOM-OGG c/o ESRF
71 Avenue des Martyrs, Grenoble, France

Responsabile editoriale: Francesco d'Acapito
(dacapito@iom.cnr.it)

Editing: Roberta De Donatis
(roberta.dedonatis@cnr.it)

ISSN 2553-9248

LISA

Annual Report
2018

Abstract

This document resumes the activity of the Italian CRG beamline at ESRF (LISA project) during year 2018. The latest news from the beamline are presented as well as statistic data about scientific activity, highlight experiments and publications.

Keywords

Italian beamline at ESRF, BM08

LISA project

X-ray Absorption Spectroscopy

<i>p. 3</i>	1. Foreword
<i>p. 5</i>	2. News from the beamline <ul style="list-style-type: none"><i>2.1 New opportunities from increased spatial resolution ... p. 5</i><i>2.2 Ardesia detector ... p. 7</i><i>2.3 Total Electron Yield detector ... p. 8</i><i>2.4 New device for accurate temperature dependent XAFS measurements ... p. 9</i><i>2.5 Fast pulsed laser ... p. 10</i>
<i>p. 11</i>	3. Highlights <ul style="list-style-type: none"><i>3.1 Optical Properties and Bismuth Redox in Bi-Doped High-Silica Al-Si Glasses ... p. 11</i><i>3.2 The puzzling structure of Cu_5FeS_4 (bornite) at low temperature ... p. 13</i><i>3.3 XEOL-XAFS Investigation of Highly Luminescent Few-atom Silver and Lead Clusters Confined in LTA zeolites ... p. 15</i><i>3.4 Two-step growth mechanism of supported Co_3O_4-based sea-urchin like hierarchical nanostructures ... p. 17</i><i>3.5 Formation and evolution of crystal and local structures in nanostructured $\text{Ln}_2\text{Ti}_2\text{O}_7$ (Ln = Gd - Dy) ... p. 19</i>
<i>p. 21</i>	4. Reports from the Block Allocation Groups <ul style="list-style-type: none"><i>4.1 Understanding Charge Transfer and Redox Cascade Phenomena in Photoelectrode Architectures by operando XAS ... p. 21</i><i>4.2 Correlation between atomic ordering and magnetic properties in binary magnetic alloys ... p. 24</i><i>4.3 XRF and XANES spectra for studies of cryospheric science at the LISA beamline ... p. 27</i>
<i>p. 30</i>	5. 2018 Publications
<i>p. 32</i>	6. Contacts
<i>p. 32</i>	7. Contributors to this issue



Ribbon cutting ceremony held on Nov 26th 2018.

*From the left: the chairman of the ESRF Council Miguel Angel Garcia-Aranda, the acting director of the "Physical sciences and technologies of matter" CNR department Corrado Spinella, the responsible of LISA Francesco d'Acapito and the chairman del Scientific Advisory Committee of ESRF Edgar Weckert.
Picture Chantal Argoud, ESRF.*

Dear all,

It is a great pleasure for me to announce you that the user program of the LISA beamline restarted early this year. The mirrors have been finally installed and since April 2017 LISA is open to users with the complete instrumentation. About three weeks of beamtime have been dedicated to the commissioning of the beamline and the results have been collected in a paper in press on the Journal of Synchrotron Radiation (DOI: 10.1107/S160057751801843X). The main result is that all the relevant parameters of the beamline closely follow the design targets. The beamline has been officially inaugurated on November 26th at the presence of the ESRF management (Francesco Sette, Luis Sanchez-Ortiz, Harald Reichert, Jean Susini, Pantaleo Raimondi), the Italian Delegation to the Council (Speranza Falciano, Elisa Molinari, Antonella Tajani) and representatives of ESRF and LISA staff.

During year 2018, 30 experimental sessions have been carried out at LISA in different fields like environmental sciences, materials for electronics, photo-chemistry among others and the 3 BAG projects have been successfully terminated. 24 papers related to studies conducted at the beamline have been published. The papers have reported on studies on luminescent materials (with a noticeable publication of a contribution on the journal 'Science'), batteries, nanostructured materials just to cite a few topics.

New instruments have been installed and are now available for users. An additional energy-resolving detector for X-ray fluorescence at low energy ($E < 15$ keV) has been commissioned. It is a 4 channels Silicon Drift Detector from the ARDESIA project that is the result of a collaboration between LISA, Politecnico di Milano and INFN. For experiments in pump and probe mode a fast (< 1 ns) pulsed laser has been purchased in the framework of the NEWLI PRIN project.

LISA has moreover continued the activity of host laboratory and tutor for young scientists and this year we have welcomed for 9 months Andrea Fantin from the Technische Universität Berlin (Germany) and for three months Shehab Esmail Mohammed Ali from Suez Canal University (Egypt).

They have both actively contributed to the beamline scientific life by developing parts of instrumentations as described in the following sections.

Next year will be dedicated to the preparation of the beamline to the new EBS ring. The beam direction will be changed by a few cm outwards respect to the ring and all the components need be displaced accordingly. The moving and alignment operations will be carried out in tight collaboration with ESRF technical services. Looking forward to see X-rays again, at present the Users Mode is scheduled to resume in late August 2020.

Pictures from the inauguration



The ESRF DG, F. Sette (right), during his speech. In the background from the left: some delegates to the Council B. Blair (UK), A Tajani and E. Molinari (I), the machine director P. Raimondi and the LISA responsible, F. d'Acapito.



A toast for LISA.

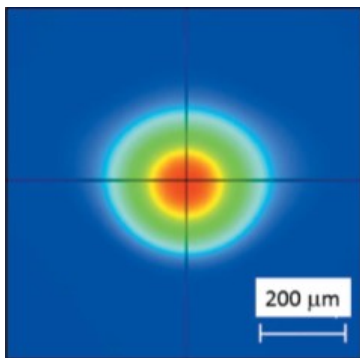
From the left: G.O. Lepore (IOM-OGG), E. Dettona (ESRF), P. Ghigna (U. Pavia), F. d'Acapito (IOM-OGG), A Vertova (U. Milano), M. Fracchia (U. Pavia), A. Fantin (T.U. Berlin), S. E. Ali (Suez Canal U.), A. Puri, F. la Manna (IOM-OGG)

2. News from the beamline

2.1. New opportunities from increased spatial resolution

G. O. Lepore (CNR-IOM-OGG)

The beam provided by the new optics is extremely stable with movements comprised within the 10% of the beam size over an angular range of 30° for both monochromator crystals pairs. The new toroidal mirror, placed downstream the monochromator, focalizes the beam on a roughly circular spot with a diameter smaller than $200\ \mu\text{m}$ FWHM (Figure 1). Such beam size, shape and stability allow a considerable increase in the beamline possibilities in terms of spatial resolution.



The beam can currently be cut down to $\sim 100\ \mu\text{m}$ (H) $\times 60\ \mu\text{m}$ (V) with a flux in the range of $\sim 10^{10}\ \text{ph s}^{-1}$. The smaller beam size opens the way to the investigation of complex heterogeneous samples in a broad variety of scientific fields, ranging from environmental sciences to materials sciences and archeometry.

Fig. 1: Experimental beam spot.

It is indeed possible to image elemental distributions with sensitivity to trace elements down to a few ppm. Moreover, the chemical state of a selected element can be determined by means of standard punctual XAS measurements or by studying the distribution of the fluorescence emission intensity in a selected region of interest (ROI) at a specific energy.

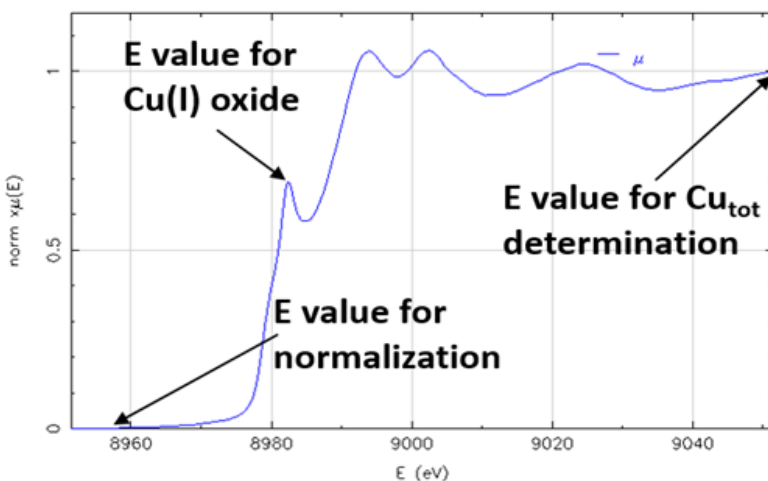


Fig. 2: XANES Cu K edge spectrum of the investigated tile (red region of the sample in Figure 3a). The energy values chosen for the XRF maps of Figure 3 are indicated by arrows.

As an example, Figure 2 shows the XANES Cu K-edge spectrum of a thin polished section of a medieval mosaic tile (Figure 3a), part of the original façade of the Santa Maria del Fiore cathedral in Florence (Italy). Different maps of the whole tile were measured at specific energy values: a first below the edge jump ($8.9\ \text{KeV}$, map I), in order to normalise the total intensity; a second at $\sim 9.1\ \text{KeV}$, able to trace the overall Cu content in the sample (map II); a third, located at the energy value of the main feature attributable to Cu(I) oxide, i.e. at $\sim 8.9823\ \text{KeV}$ (map III).

From the comparison of the three raw maps, two different combined maps can be obtained, one revealing to the total Cu content distribution in the sample (Figure 3b), the other revealing the differences in oxidation and structural features of Cu distribution in the sample (Figure 3c).

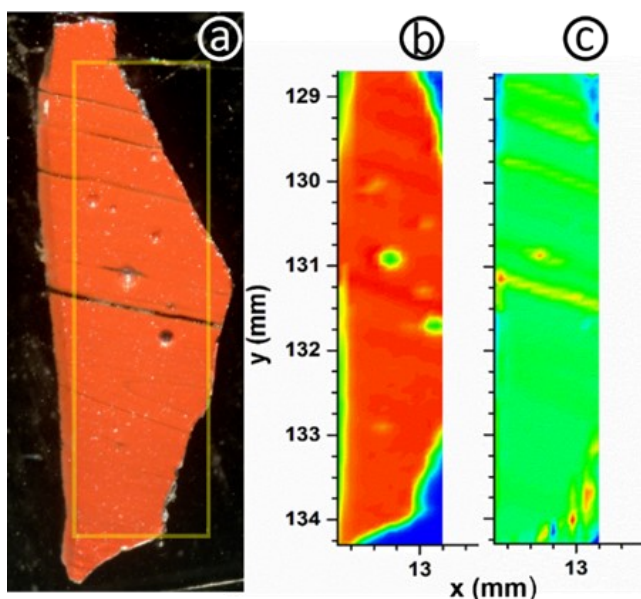


Fig. 3: a) optical micrograph of the investigated sample; b) total Cu content: image obtained combining map I and map II; c) redox/structural Cu contrast: image obtained combining map III and map I.

Another interesting consequence relies in the possibility, previously precluded due to the millimetric size of the beam, to study small crystals. This aspect is particularly interesting in the field of earth and environmental sciences, where the availability of the samples can be limited and where the interest on the sample may require its full preservation. As an example, Figure 4 reports collected XAS spectra on a single riebeckite fiber (from Puri et al., 2019) and of a single crystal of piccolite (Camara et al., 2017) at Fe and Mn K-edges, respectively.

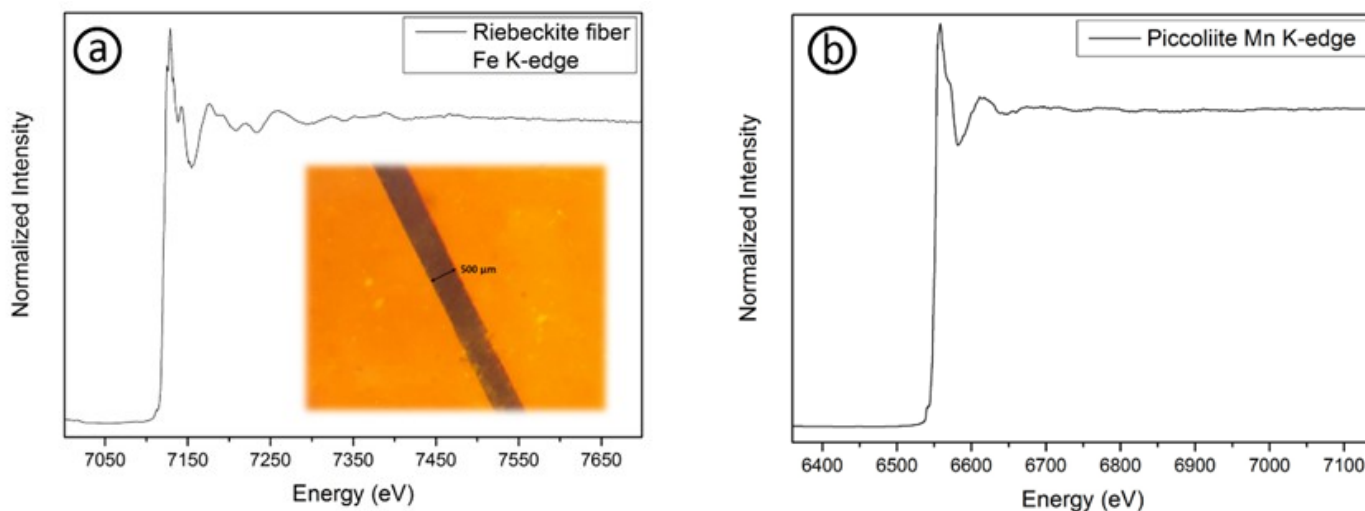


Fig. 4: a) Fe K-edge XAS spectrum of the riebeckite fiber ($\sim 500 \mu$ diameter) shown in the inset; b) Mn K-edge XAS spectrum of a piccolite single crystal (size $\sim 150 \times 200 \mu^2$).

References: [Cámara, F. et al. (2017) CNMNC Newsletter **37**, 741 – Min. Mag. **81**, 737–742; Puri et al. (2019) Condens. Matter **4**, 12.]

2.2. Ardesia detector

A. Puri (CNR-IOM, Grenoble)

A new multielement Silicon Drift Diode (SDD) detector from the project ARDESIA is now available at LISA. This detector is particularly effective for X-ray Fluorescence (XRF) and X-ray Absorption Spectroscopy (XAS) experiments at $E < 15$ keV, offering high count rates (up to 1Mcps/channel) and high energy resolution (down to 150 eV FWHM).

The detection module consists of 2×2 -pixel monolithic SDD coupled with a 4-channel version of the CUBE CMOS preamplifier (Bellotti et al., 2018). The instrument has been realized to fit inside the sample chamber with a finger-like structure and allows to operate in vacuum. A built-in Peltier system grants proper cooling (-30 °C) under static vacuum condition (10^{-2} mbar).

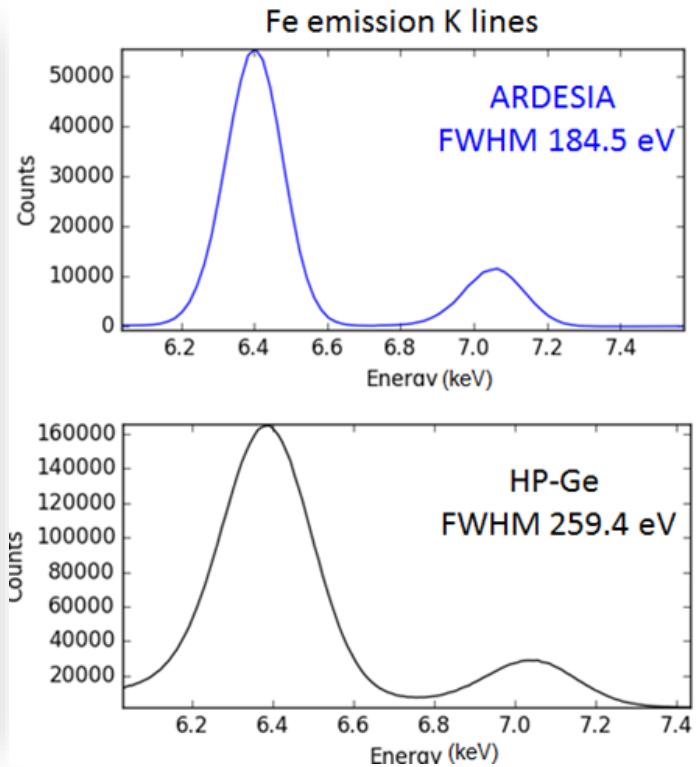


Fig. 1: Left): Photograph of the ARDESIA snout mounted on a vacuum flange. Right): Energy resolution comparison between ARDESIA (upper panel) and the HP-Ge detector available at LISA (lower panel), at Fe emission K lines. The energy resolution gain is $\approx 30\%$ at 6.4 keV.

Bellotti, G., Butt, A.D., Carminati, M., Fiorini, C., Bombelli, L., Borghi, G., Piemonte, C., Zorzi, N., Balerna, A., 2018. IEEE Trans. Nucl. Sci. 65, 1355–1364. DOI 10.1109/TNS.2018.2838673

2.3. Total Electron Yield detector

A. Fantin (TU-Berlin), A. Puri (CNR-IOM, Grenoble)

A new apparatus for XAS measurements in Total Electron Yield mode has been realized. It allows to probe up to six samples, with the possibility to collect simultaneously fluorescence and TEY spectra. The main characteristics are:



- Secondary electrons collector, anode at $V \approx 17$ V
- He gas electron multiplier
- Multi-sample holder (up to six specimens)

The device is placed in the measurement chamber filled by He gas (0.8 bar) for signal amplification. The specimens are placed onto the carbon tapes (cf. Fig.1) for a better connection to ground. The incident X-ray beam (red dashed line) passes through the front window and impinges directly upon the sample. The Auger electrons emitted from the sample surface ionize the He atoms creating a cascade. The total electron yield (Auger and secondary electrons) is collected by the anode (right-hand side of Fig.1) kept at a moderate voltage ($\approx +17$ V in the present case). The resulting current is converted to a voltage signal via a Keithley amplifier. Due to the short mean free path of the electrons, TEY measurements allow to probe a material close to its surface, this is useful in case of thin films on a substrate, thick samples or when fluorescence measurements are not possible because of the large emission background from the matrix or spurious Bragg reflections. Since about 30eV is required to create an ion pair in He, there is a gain factor equal to Auger energy/30, i.e. about 100-200 for 3d transition metal elements, realistic case for the investigated compositionally complex alloy –CCA– $\text{Al}_8\text{Cr}_{17}\text{Fe}_{17}\text{Co}_{17}\text{Ni}_{33}\text{Cu}_8$.

Fig. 1: Total Electron Yield device

An example of one spectrum collected in Total Electron Yield mode is presented in the following Fig. 2. The measuring time was about 40 minutes (3sec/step)

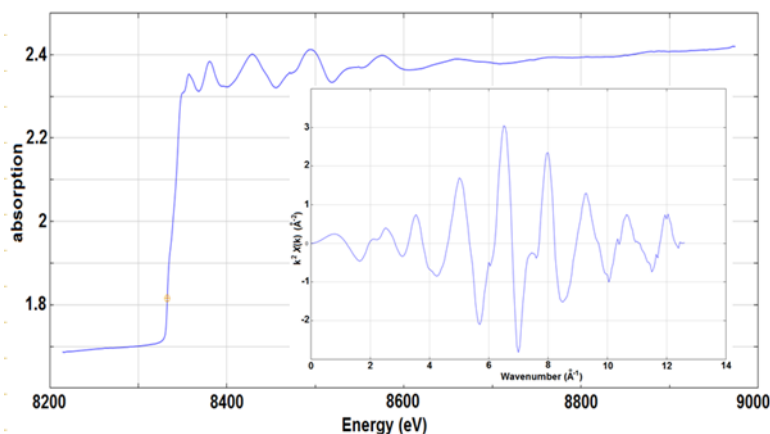


Fig. 2: Single X-ray absorption spectrum of the CCA single crystal $\text{Al}_8\text{Cr}_{17}\text{Fe}_{17}\text{Co}_{17}\text{Ni}_{33}\text{Cu}_8$ measured at the Ni-K edge with the Total Electron Yield device shown in Fig. 1, as a function of the energy of the incident X-ray photons. In the inset, the normalized $\chi(k)$ is presented as a function of the photoelectron wavenumber k . The function $\chi(k)$ is k^2 -weighted. The limited measured energy range is due to the Cu-K edge at 8979 eV.

2.4. New device for accurate temperature dependent XAFS measurements

Shehab E. Ali (Suez Canal University), G.O. Lepore (CNR-IOM, Grenoble)

A new cryostat has been installed in the sample chamber of the experimental hutch 1 (EH1) of LISA. The cryostat, manufactured by Air Liquid (France), is dedicated to accurate temperature-dependent EXAFS measurements. Measurements will be mainly carried out in transmission mode since EH1, given the new beamline optics, will be used for experiments which require a wide defocused beam.

The device allows to reach temperatures from 80K up to 525K and it is equipped with a gold-plated copper sample holder in order to maximize thermal conductivity. The sample holder allows to mount up to four samples, the vertical range of movement is 10 cm and the manipulator can be rotated by 180° around the vertical axis.

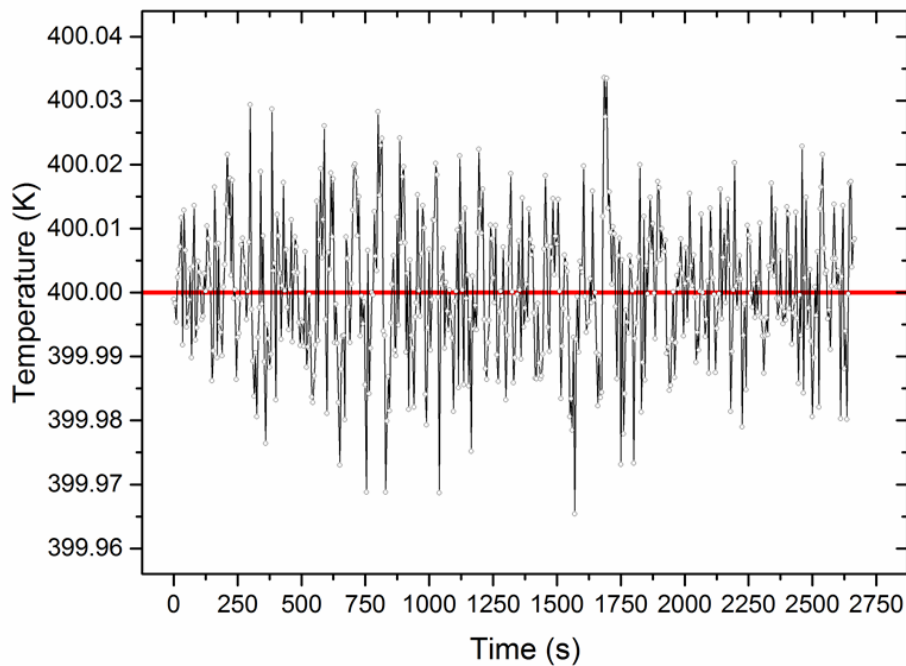


Fig. 1: Temperature stability during a whole I K-edge (33169 eV) XAFS scan, temperature set point is 400 K (red line).

A PT100 temperature detector is used to monitor the temperature of the sample holder, which is cooled by a flux of cold N₂ gas (down to Liquid Nitrogen T) and heated by a resistance. The power heating unit has been developed by the electronic service of the physics department of the University of Trento. The temperature is controlled via a Eurotherm unit, allowing remote control via RS232 port with standard communication protocols; the temperature control is currently integrated as a pseudo-motor in the SPEC sessions of LISA.

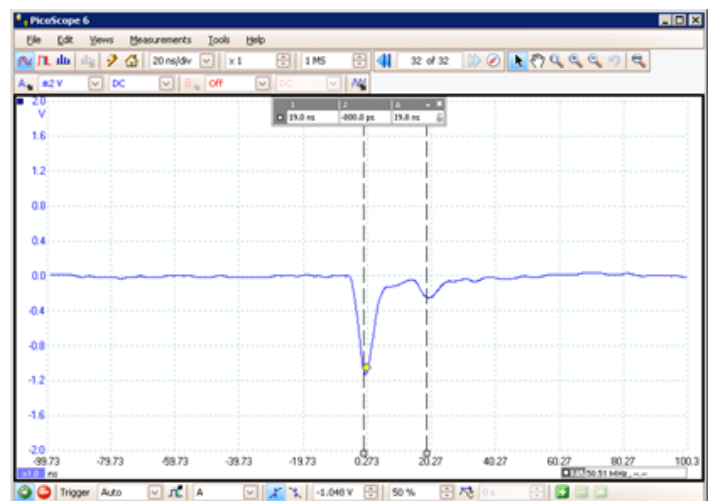
Some general-purpose additional connections are available to the users, allowing to install additional items such as temperature sensors, electrical connections for total electron yield detection, rotating/vibrating supports.

As it is possible to notice from Figure 1, the device provides a very precise temperature control on the mounted samples with a temperature stability of approximately ± 0.03 K.

2.5. Fast pulsed laser

F. d'Acapito (CNR-IOM, Grenoble)

LISA participates to the NEWLI PRIN (2015CL3APH) project aiming to develop experimental methods for investigating transient states of matter. The idea at the base of the LISA contribution is to realize stroboscopic pump-and-probe XAS experiments where the pump is a light pulse that excites the sample synchronously with the X-ray flashes from the storage ring. At this purpose a diode laser has been purchased and successfully tested on the beamline. The laser (mod. PiLas by A.L.S. GmbH) can provide pulses of wavelength $\lambda = 404$ nm, duration $t = 1$ ns of energy $E = 465$ pJ at a repetition rate of 5.6 MHz corresponding to the machine frequency in 16 bunches mode. The output of the laser is sent to an optic fibre that enters the sample vacuum chamber and shines the sample through a focusing lens. The beam spot is about 2mm for an easier alignment with the X-ray beam. Using a fast photomultiplier placed at the sample location it is possible to detect at the same time the X-ray and UV pulses and set the delay parameters between the pump and the probe beams.



The fast laser available at LISA. Left: the control unit that can be triggered with the pulses from the BCDU8 unit the programmable synchronized pulse generator. Left the laser head with the output on optic fibre.

Scope trace of the output of the photomultiplier shined at the same time by the UV (deeper peak, at the left) and X-ray pulses (smaller peak, on the right). In this way the interval between the pump and the probe beams can be easily measured and changed.

XAS experiments in pump and probe mode stroboscopic mode on Ag nanoparticles on CeO₂ have been carried out during the 16b modes in 2018. XAS spectra were collected with different time intervals between the UV and X-rays from 0.5 to 150 ns. The related data are currently under analysis.

Optical Properties and Bismuth Redox in Bi-Doped High-Silica Al-Si Glasses

A. Veber¹, M.R. Cicconi¹, A. Puri², D. de Ligny¹

¹WW3-University of Erlangen-Nuremberg, Germany, ²CNR-IOM-OGG Grenoble

Thermal expansion of solids is critical in many technological applications and its control is a key issue for the materials design. In this regard, the occurrence of negative thermal expansion (NTE) materials offers a promising possibility to control the thermal expansion. Herein, we demonstrate that the thermal expansion of YFe(CN)₆-based Prussian blue analogues can be switched from giant negative to positive by introducing guest molecules (H₂O) and ions (K⁺) into the void spaces of its framework structure.

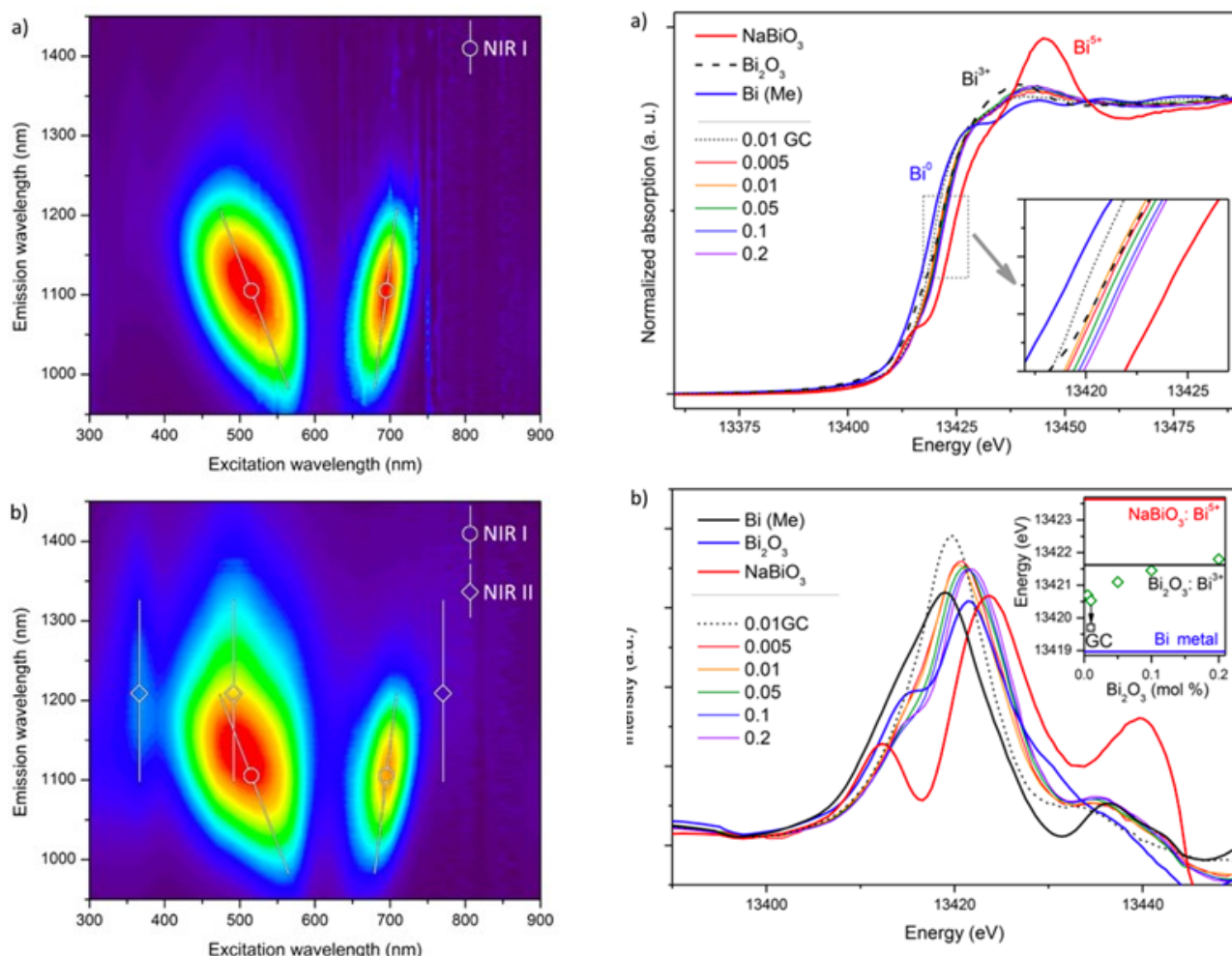


Fig. 1: Normalized 2D excitation–emission plots for glasses doped with a) 0.005 mol% Bi₂O₃, and b) 0.2 mol% Bi₂O₃.

Fig. 2: a) Normalised XANES spectra of Bi model compounds and glasses. b) First derivative of the spectra and edge position

A set of glasses $95.5\text{SiO}_2\text{-}4.5\text{Al}_2\text{O}_3\text{-}x\text{Bi}_2\text{O}_3$ ($x = 0; 0.005; 0.01; 0.05; 0.1; 0.2$ mol%) were synthesized using a conventional melt- quenching technique in air, or under reducing conditions (label GC). NIR luminescence property variations depending on Bi-concentration can be observed from comparison of 2D excitation–emission plots measured for 0.005 and 0.2 mol% Bi-doped glasses, as shown in Figure 2.3.1.1. XANES spectra were collected at the Bi L_{III}-edge (13419 eV) in FY by using a 12-element high- purity Ge detector, in the energy range 13200–13650 eV. Three crystalline compounds were used as references, respectively for Bi⁰ (metallic foil), Bi³⁺ (Bi₂O₃) and Bi⁵⁺ ions (NaBiO₃). XANES data for Bi-doped glasses show that bismuth redox equilibrium shifts depending on its concentration (Figure 2.3.1.2).

Lower Bi₂O₃ contents favor the stabilization of more reduced Bi species with formal valency <+3, although Bi³⁺ ions apparently dominate in glasses melted in air. Syntheses under reducing conditions enhance the content of reduced Bi⁺ species, without forming metallic particles. Luminescence in the NIR region at low Bi concentrations can be explained by stabilization of the Bi⁺ ion in the glass structure.

Publication: Veber et al., J. Phys. Chem. C 122 (2018), 19777.

The puzzling structure of Cu_5FeS_4 (bornite) at low temperature

A. Martinelli¹, G. O. Lepore², F. Bernardini³, A. Giaccherini⁴, F. Di Benedetto⁴

¹SPIN-CNR, ²OGG-IOM-CNR, ³University of Cagliari, ⁴University of Florence

Bornite, Cu_5FeS_4 , is a widespread sulfide mineral being credited as one of the most important Cu ores (Borgheresi et al. 2018). More recently, this mineral has raised a relevant interest in Materials Science, due to its thermoelectric properties (Qiu et al. 2014). Only a deeper knowledge of the structural and crystal chemical features of this mineral will allow its final exploitation as material for the energy conversion. With this respect, some questions are still open: the localisation of Fe in the structure, the low temperature magnetic structure and the possible occurrence of a low temperature polymorph.

The structural properties of Cu_5FeS_4 (mineral sample) were investigated in the thermal range 10–275 K. The sample, kindly provided by the Natural History Museum of the University of Florence (Catalogue n° 14975), was collected at the Cu-sulphide ore of Montecatini Val di Cecina (Tuscany, Italy). X-ray powder diffraction (XRPD) data ($\lambda = 0.35417 \text{ \AA}$) were collected between 275 K and 10 K at the ID22 high-resolution powder diffraction beamline of the European Synchrotron Radiation Facility (ESRF). Pair distribution function (PDF) analysis was carried out using the same XRPD data. X-ray Absorption Spectroscopy (XAS) measurements at the Fe K-edge (7112 eV) were performed at the LISA beamline (BM08) of ESRF.

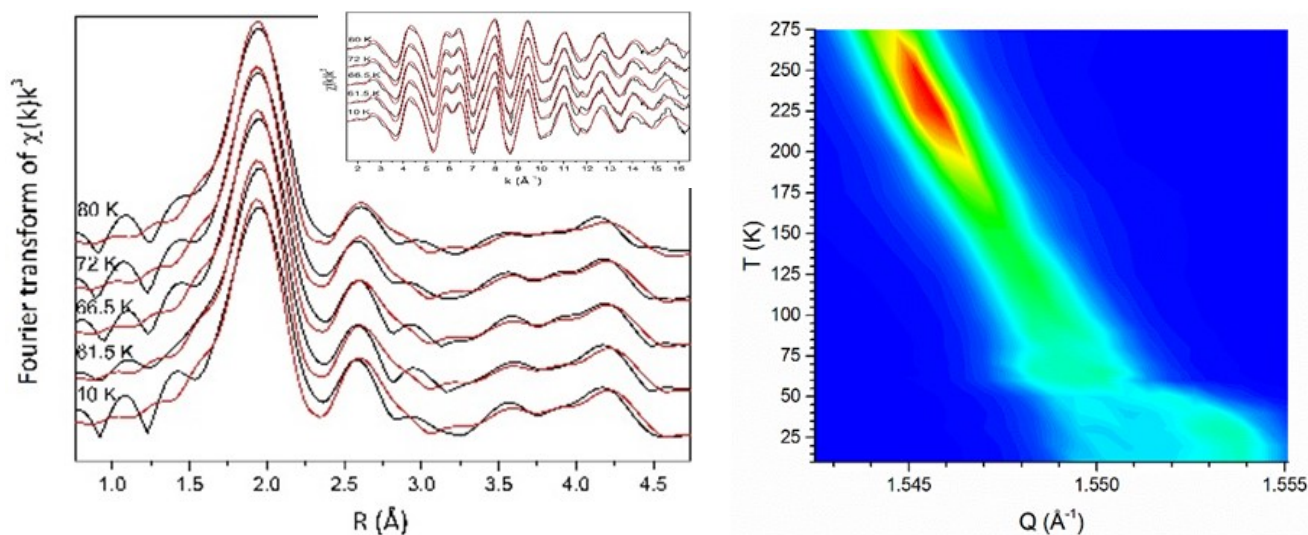


Fig. 1: Fe K-edge EXAFS (up) and Fourier transform (down) of bornite measured at different temperatures. Solid lines are data, red lines are fits.

Fig. 2: Evolution of the diffraction peaks at $Q \sim 1.5 \text{ \AA}^{-1}$ in the thermal range 275 – 10 K.

At 275 K, bornite crystallizes in the orthorhombic space group $Pbca$; the crystal structure consists of an ordered arrangement of anti-fluorite (structural sites: M1, M2, M3, M4, M5, M6, M7, M8) and sphalerite (structural sites: M9, M10, M11, M12) type structural units, resulting from the ordering of vacancies, Cu and Fe atoms in the interstices of the face centred lattice formed by S atoms.

Even though the direct check of the cationic ordering at the structural M sites is prevented on account of the similar X-ray scattering lengths characterizing Cu and Fe atomic species, crystal chemical considerations based on both XRPD and EXAFS data strongly point, as already suggested by Koto & Morimoto (1975) towards and ordering of Fe atoms in the M4 and M5 sites. M4 and M5 show the smallest distortional parameters, other than the shortest M-S average bond length; in addition, the Fe-S distance obtained by the EXAFS analysis perfectly agrees with the M-S average bond length observed in M4 and M5 (~ 2.30 Å). Vacancies are found in the sphalerite type unit, together with Cu atoms, in tetrahedral coordination, but heavily displaced from the centres. One of the Cu atoms is displaced towards a nearly planar 3 coordination (site M10). Below ~65 K, selected peak broadening is observed, clearly highlighting the occurrence of a structural transition (Figure 2). Noteworthy, the analysed sample displays an antiferromagnetic transition at about the same temperature (~67.5 K). The primary active mode yielding the observed ordered structure corresponds to the irreducible representation labelled Γ_2^- , with wave vector (0,0,0); as a result a 1st order Pbc_a → Pca₂₁ structural transition takes place. Pair distribution function analysis evidences strong discrepancies between the local and the average structure at both 275 K and 10 K. Concluding, the present study addresses the Fe localisation in the structure, finally attributed to the M4 and M5 sites, and it identifies and describes for the first time the fourth polymorph structure of bornite.

Publication: [Acta Crystallographica **B74** (2018), 405.]

References: [Borgheresi, M., Di Benedetto, F., Romanelli, M., Reissner, M., Lottermoser, W., Gainov, R. R., Khassanov, R. R., Tippelt, G., Giaccherini, A., Sorace, L., Montegrossi, G., Wagner, R. & Amthauer, G. (2018). Phys. Chem. Mineral. 45, 227–235.

Koto, K. and Morimoto, N. Acta Cryst. B31 (1975), 2268.

Qiu, P., Zhang, T., Qiu, Y., Shi, Xun C., Lidong Energy Environ. Sci. 7(12), (2014), 4000-4006.]

XEOL-XAFS Investigation of Highly Luminescent Few-atom Silver and Lead Clusters Confined in LTA zeolites

D. Grandjean¹, S. Aghakhani¹, E. Coutino-Gonzalez², W. Baekelant², F. D'Acapito³, M.B. J. Roeffaers⁴, J. Hofkens², P. Lievens¹

¹Laboratory of Solid State Physics and Magnetism, KU Leuven, Celestijnenlaan 200D, B-3001 Leuven, Belgium.

²Molecular Visualization and Photonics, KU Leuven, Celestijnenlaan 200F, B-3001 Leuven, Belgium.

³CNR-IOM-OGG, ESRF, LISA Collaborating Research Group, Grenoble, France.

⁴Centre for Surface Chemistry and Catalysis, KU Leuven, Celestijnenlaan 200F, B-3001 Leuven, Belgium

Few-atom metal clusters confined inside Linde Type A (LTA) zeolite framework display unique electronic, catalytic, and optical properties. We have prepared Silver (AgCLs) and Lead clusters (PbCLs) inside LTA zeolite displaying high and tunable photoluminescent quantum efficiencies and used x-ray excited optical luminescence-x-ray absorption fine structure (XEOL-XAFS) at LISA-BM08 beamline of the ESRF to unravel their structures and the origin of their luminescence.

Origin of the bright photoluminescence of few-atom silver clusters confined in LTA zeolites (1)

We have characterized the bright green luminescent AgCLs confined in partially exchanged heat-treated $\text{Ag}_3\text{K}_9\text{-LTA}$ by a combination of XEOL-XAFS (Figures 1A-D), time-dependent-density functional theory calculations, and time-resolved spectroscopy. A mixture of tetrahedral $\text{Ag}_4(\text{H}_2\text{O})_x$ ($x = 2$ and $x = 4$) clusters at the center of a fraction of the sodalite cages were identified (Figures 1E-J).

Their optical properties originate from a confined two-electron superatom quantum system with hybridized Ag and water O orbitals delocalized over the cluster. Upon excitation, one electron of the s-type highest occupied molecular orbital is promoted to the p-type lowest unoccupied molecular orbitals and relaxes through enhanced system intercrossing into long-lived triplet states.

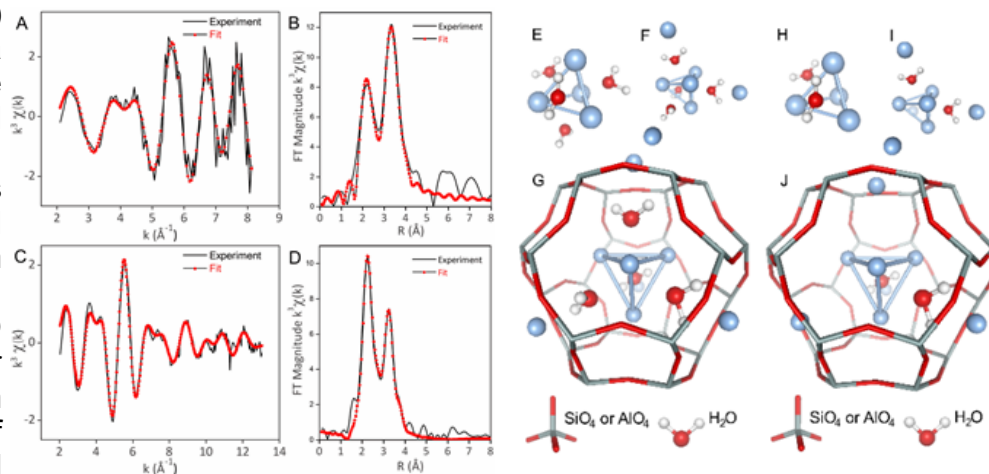


Fig. 1: XEOL-detected (A) and transmission-detected (C) k^3 -weighted Ag K-edge EXAFS with the phase corrected XEOL-detected FT (B) and transmission-detected FT of heat-treated $\text{Ag}_3\text{K}_9\text{-LTA}$ (D) best fits. Structures of $\text{Ag}_4(\text{H}_2\text{O})_4$ and $\text{Ag}_4(\text{H}_2\text{O})_2$ (E and H), including Ag_R cations (F and I) and embedded in the sodalite cage (~ 0.66 nm free diameter) (G and J) respectively.

Shaping the Optical Properties of Silver Clusters Inside Zeolite A via Guest-Host-Guest Interactions (2)

The luminescent properties of $\text{Ag}_4(\text{H}_2\text{O})_x$ clusters in LTA zeolite was tuned by co-exchanging Ag and a variable amount of Li co-cations in the zeolite framework. A strong emission color shift directly correlated with the Li content was attributed to precise changes in the cluster structure and environment by XEOL-XAFS and transmission-EXAFS (Tr-EXAFS).

In $\text{Ag}_1\text{Li}_x\text{Na}_{12-x}\text{LTA}$ zeolite the tetrahedral AgCLs are surrounded by Li cations positioned at short distances of 2.70–2.73 Å in the axis of the 4-membered ring inside the sodalite cage. Upon increasing Li loading the average number of Li ions surrounding the AgCLs was shown to vary from 4 to 6. The increase in the number of Li cations with large Coulombic forces and small ionic size in the vicinity of the clusters and the concomitant shortening of the intracuster Ag-Ag distances and of the zeolite lattice parameter allowed a fine tuning of the Ag-zeolites' emission properties.

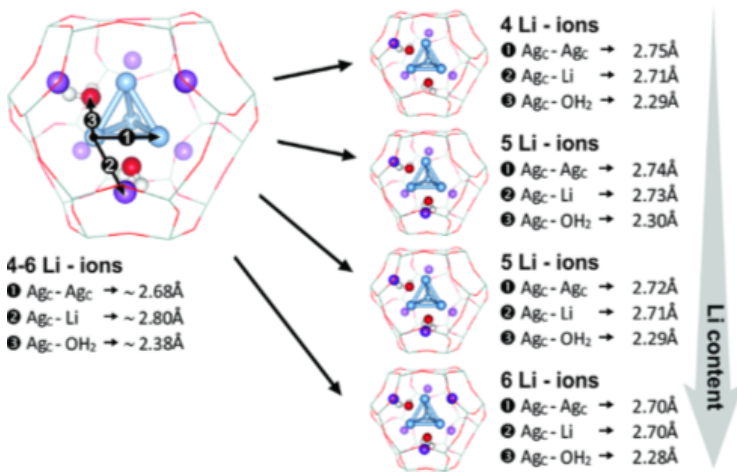


Fig. 2: (A) Tetrahedral AgCL structures confined inside the sodalite cages of $\text{Ag}_1\text{Li}_x\text{Na}_{12-x}\text{LTA}$ as determined by Tr- (left) and XEOL-EXAFS (right), respectively, showing the number of surrounding Li^+ and distance between the Ag_c (sky blue) and Ag_c (1), Li^+ (purple; 2), and the oxygen of the water ligands (red; 3) for the Ag_1 -exchanged $\text{Li}_0\text{Na}_{12}$ (upper).

Confinement of Highly Luminescent Lead Clusters in Zeolite A (3)

We demonstrated by XEOL-XAFS and Tr-EXAFS the self-assembly and confinement of highly luminescent PbCLs in $\text{Pb}_{0.5}\text{Na}_{11}\text{-LTA}$ zeolites. Tetrahedral Pb_4 clusters with unusually short Pb-Pb distances of ca. 2.90 Å and hydroxyl ligands were identified as responsible for the deep-blue luminescence with quantum efficiencies up to 69% observed in Pb-LTA. Upon thermochemical treatments a swap of PbCLs ligands from water molecules to hydroxyls and atomic oxygens was demonstrated. Detailed structures of the different PbCLs based on XEOL-XAFS will be published soon.

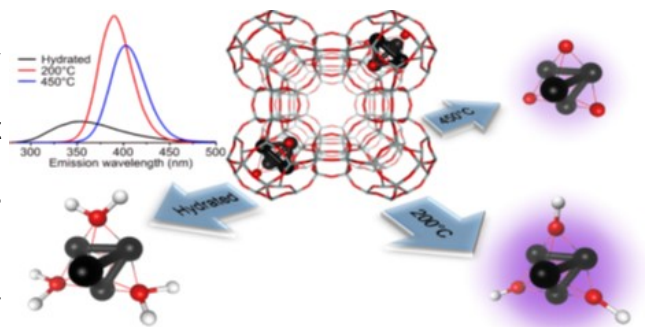


Fig. 3: Structures of $\text{Pb}_4(\text{H}_2\text{O})_4$, $\text{Pb}_4(\text{OH})_2$ and $\text{Pb}_4(\text{OH})_2$ free and embedded in the sodalite cage with their respective emissions curves

Publications:

- (1) Grandjean, D.; Coutino-Gonzalez, E.; Cuong, N. T.; Fron, E.; Baekelant, W.; Aghakhani, S.; Schlexer, P.; D'Acapito, F.; Banerjee, D.; Roeffaers, M. B. J.; Nguyen, M. T.; Hofkens, J.; Lievens, P., *Science* 2018, 361 (6403), 686-689.
- (2). Baekelant, W.; Aghakhani, S.; Coutino-Gonzalez, E.; Kennes, K.; D'Acapito, F.; Grandjean, D.; Van der Auweraer, M.; Lievens, P.; Roeffaers, M. B. J.; Hofkens, J.; Steele, J. A., *J Phys Chem Lett* 2018, 9 (18), 5344-5350.
- (3). Baekelant, W.; Aghakhani, S.; Coutino-Gonzalez, E.; Grandjean, D.; Kennes, K.; Jonckheere, D.; Fron, E.; d'Acapito, F.; Longo, A.; Lievens, P.; Roeffaers, M. B. J.; Hofkens, J., *J Phys Chem C* 2018, 122 (25), 13953-13961.

Two-step growth mechanism of supported Co_3O_4 -based sea-urchin like hierarchical nanostructures

C. Maurizio ¹, R. Edla ², N. Michieli ¹, M. Orlandi ², A. Trapananti ³, G. Mattei ¹, A. Miotello ²

¹Physics and Astronomy Department, University of Padova, Italy ²Physics Department, University of Trento, Italy, ³CNR-IOM, Physics and Geology Department, University of Perugia, Italy

Supported 3D hierarchical nanostructures of transition metal oxides exhibit enhanced photocatalytic performances and long-term stability under working conditions. The growth mechanisms crucially determine their intimate structure, that is a key element to optimize their properties. We have studied the formation mechanism, induced by air annealing, of supported Co_3O_4 hierarchical sea urchin-like nanostructured catalyst, starting from Co-O-B layers deposited by Pulsed Laser Deposition (PLD). The particles deposited on the layer surface, that constitute the seeds for the urchin formation, have been investigated after separation from the underneath deposited layer (see Figure 1(a)), by X-ray diffraction, X-ray absorption spectroscopy and scanning electron microscopy. In Figure 1(b-e) the modification of the sample morphology is shown at different step of isothermal annealing, with the formation and growth of nano-needles out of spheroidal particles. Correspondingly, in Figure 1(f) the Fourier transform moduli of the EXAFS spectra recorded at Co K-edge in fluorescence mode (RT) for the full layers (red line) and particle layers (blue line) are shown.

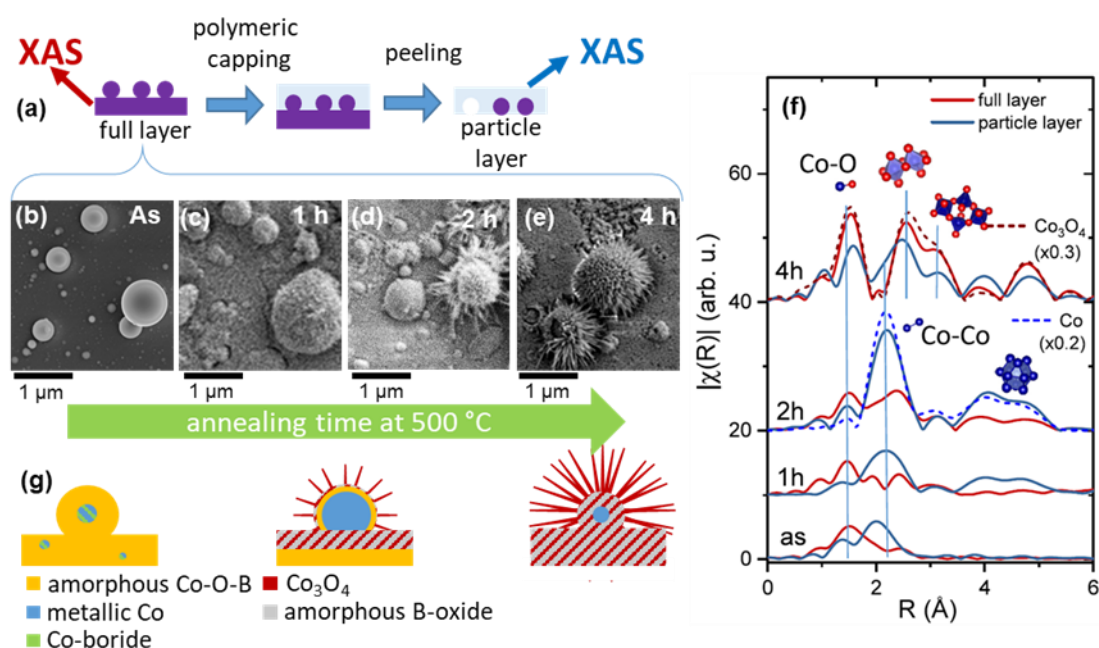


Fig. 1: (a) Sketch of the Co-O-B nanostructured samples and of the procedure used to separate the particles from the layer beneath. (b-d) SEM images of the sample after annealing at 500°C for the indicated time. (e) Fourier transform moduli of the EXAFS spectra recorded at Co K-edge from the full layers and particle layers. The spectrum of Co_3O_4 crystalline powder and of metallic Co is also shown. (f) Sketch of the structural evolution of Co-O-B deposited layers upon air annealing at 500°C, as retrieved by the XAS, XRD and SEM investigations.

As far as the particle layers are concerned, a Co-Co metal coordination is present for all the layers, that increases in the first 2h annealing and then decreased to 0. This indicates that during oxidizing annealing Co undergoes a chemical reduction, likely induced by the concomitant oxidation of boron atoms.

The coordination number of the metallic phase in the particle layer is significantly higher than for the full layer. The full layer is generally more oxidized, indicating the metallic fraction is preferentially located in the particles, likely close to the core. About the full layers, a first Co-O coordination is visible in all cases, while the metallic coordination is barely visible for annealing duration less than 2 h, and is present as a minor phase for the layer annealed for 2 h. After 4 h annealing, the spectrum is very similar to the one of Co_3O_4 . The Co-Co coordination distance is 2.45 Å for the as-deposited particle layer and 2.50–2.54 Å for the other cases, to be compared with the 2.51 Å of metallic Co and ≈ 2.4 Å of Co_2B . The short coordination distance in the as-deposited particle layer suggests that a fraction of cobalt boride is present, also in agreement with XRD results. These results, and their comparison with the results on similar PLD deposited layers, but without O and/or B, indicate a crucial role of B for the urchin formation that (i) limits Co oxidation during the deposition process and (ii) induces a chemical reduction of Co, especially in the particle core, in the first step of air annealing (2 h, 500 °C). This process is mandatory for the urchin formation. After 2 h heating Co oxidation proceeds and Co atoms outdiffuse from the Co fcc particle core likely through fast diffusion channel present in the shell and form Co_3O_4 nanoneedles. The growth of nanoneedles from the layer beneath the particles is prevented by a faster Co oxidation and a minimum fraction of metallic Co. This investigation shows how diffusion mechanisms and chemical effects can be effectively coupled to obtain hierarchical structures of transition metal oxides.

Publication: [C. Maurizio, R. Edla, N. Michieli, M. Orlandi, A. Trapananti, G. Mattei, A. Miotello, *Appl. Surf. Sci.* 439 (2018), 876.]

Formation and evolution of crystal and local structures in nanostructured $Ln_2Ti_2O_7$ ($Ln = Gd - Dy$)

V.V. Popov¹, A.P. Menushenkov^{1, *}, B.R. Gaynanov¹, A.A. Ivanov¹, F. d'Acapito², A. Puri², I.V. Shchetinin³,
M.V. Zheleznyi³, M.M. Berdnikova¹, A.A. Pisarev¹, A.A. Yastrebsev¹, N.A. Tsarenko⁴, L.A. Arzhatkina⁴,
O.D. Horozova⁴, I.G. Rachenok⁴, K.V. Ponkratov⁵

¹NRNU MEPhI, Moscow, ²CNR-IOM-OGG c/o ESRF, LISA CRG, Grenoble, ³NUST MISiS, Moscow,
⁴JSC Scientific Research Institute of Chemical Engineering, Moscow, ⁵Renishaw plc, Moscow

Since the mid-1980s the cubic pyrochlore-type complex oxides $A_2B_2O_7$ including Ln titanates attracted much attention in both fundamental and applied research due to their unique physico-chemical properties. For instance, the $Ln_2Ti_2O_7$ ($Ln = Gd, Tb, Dy$) compounds are characterized by the same crystal structure (pyrochlore-type) but quite different magnetic structures, that is, long-range ordered, spin-liquid, and spin-ice state for $Gd_2Ti_2O_7$, $Tb_2Ti_2O_7$, and $Dy_2Ti_2O_7$, respectively [1,2].

The aim of this work was to investigate the specific features of lanthanide titanates $Ln_2Ti_2O_7$ crystal and local structures during their formation and evolution. The samples were prepared by calcination of initially amorphous precursors at various temperatures. X-ray absorption spectroscopy (XAS) measurements were performed at LISA BM08. The XANES and EXAFS spectra were collected at the Ti K- and $Ln L_3$ – edges in transmission mode.

EXAFS. Crystallization of amorphous precursors upon calcination caused dramatic change in oxygen environment of rare earth elements. The splitting of the first oxygen shell into two $Ln - O$ (1) and $Ln - O$ (2) components is observed. As follows from XRD measurements, this splitting corresponds to the amorphous to pyrochlore phase transition. The exact values of the bond length versus calcination temperature, extracted from EXAFS data, are shown in Fig. 1.

XANES. The changes in the electronic structure of the local environment of titanium accompanying crystallization are clearly reflected in Ti K-edge XANES spectra (see Fig. 2). Its pre-edge features have been well studied both theoretically and experimentally (see, for example ref. [3]), but as a rule, well-crystallized materials were considered. The novelty of our approach is in the step-by-step observation of changes in pre-edge features during the transition from the amorphous to the crystalline state upon calcination. In the amorphous phase, where atoms do not have an ordered arrangement in real space and are weakly combined by the common shells, the local electron excitations inside the electronic structure of the absorber atom play the main role. That is why, the A1 and low energy part of A2 features, which correspond respectively to local quadrupole $1s$ electron transitions to the $3d-t_{2g}$ and $3d-e_g$ split by the crystal field, significantly prevail in the pre-edge structure (see spectra for calcination temperature $700\text{ }^\circ\text{C}$ in Fig. 2). During the crystallization process the nearest shells of the absorber atom local environment are formed, and their coordination numbers (CN) increase.

This facilitates the p-d hybridization of the neighboring atoms electron states through the oxygen shells of the Ti atoms local environment, which, in turn, increases the probability of nonlocal dipole-allowed $1s \rightarrow 4p$ transitions to the surrounding atoms. These processes are manifested as an emerging and further development of feature A_3 .

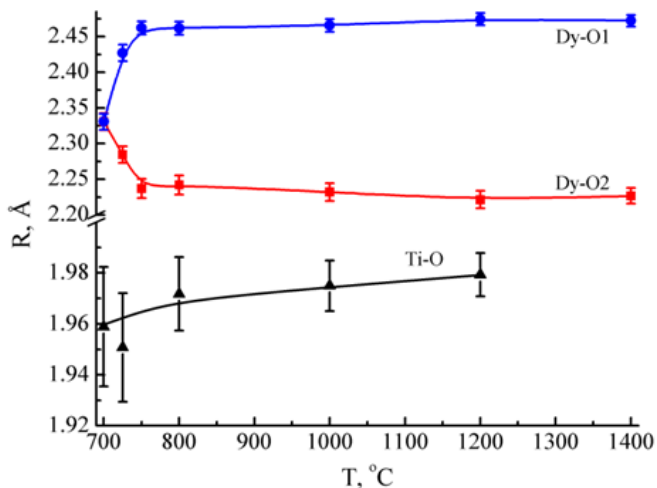


Fig. 1. Interatomic distances of the first oxygen coordination shell vs calcination temperature for $Dy_2Ti_2O_7$

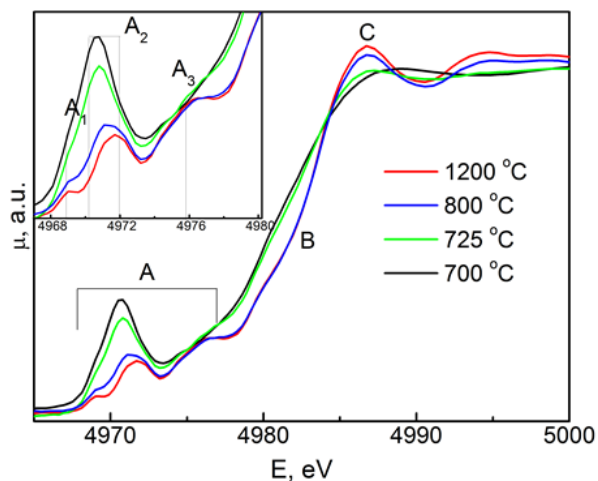


Fig. 2. K-Ti edge XANES spectra for $Dy_2Ti_2O_7$ powders after calcinations of Dy-Ti precursor at temperatures of 700, 725, 800, and 1200 °C. The pre-edge region is shown in the inset

In conclusion, we have established that both EXAFS and XANES spectroscopy provide the sensitive markers of changes in $Ln_2Ti_2O_7$ local crystal and electronic structure upon amorphous to pyrochlore transition. In particular, the observed splitting of the first Ln -O shell in the FT modulus of Ln L_3 -edge EXAFS spectra appears to be the reliable indicator of the ordered pyrochlore structure formation, while the changes in the pre-edge region in the Ti K-edge XANES spectra reflect the process of the $Ln_2Ti_2O_7$ electronic structure formation.

Publication: [J. Alloys Compd. 746 (2018) 377-39, doi:10.1016/j.jallcom.2018.02.263]

References:

- [1] J. Gardner et al., Rev. Mod. Phys. 82, 53 (2010).
- [2] T. Lummen et al., Phys. Rev. B 77, 214310 (2008).
- [3] F.Farges et al., Phys. Rev. B 56, 1809 (1997).

Understanding Charge Transfer and Redox Cascade Phenomena in Photoelectrode Architectures by operando XAS

M. Fracchia¹, A. Visibile², T. Baran³, E. Achilli¹, F. Malara⁴, V. Cristini⁵, A. Naldoni⁶, Alberto Vertova², S. Caramori⁵, E. Ahlberg⁷, S. Rondinini², P. Ghigna¹, A. Minguzzi^{1,2}

¹Dipartimento di Chimica, Università degli Studi di Pavia, Viale Taramelli 13, 27100 Pavia, Italy

²Dipartimento di Chimica, Università degli Studi di Milano, Via Golgi 19, 20133 Milano, Italy

³SajTom Light Future, Węzerów 37/1, 32-090 Węzerów, Poland

⁴CNR – Istituto di Scienze e Tecnologie Molecolari, Via C. Golgi 19, 20133 Milano, Italy

⁵Dipartimento di Scienze Chimiche e Farmaceutiche, Università degli Studi di Ferrara, Via Luigi Borsari 46, 44121, Ferrara, Italy

⁶Regional Centre of Advanced Technologies and Materials, Faculty of Science, Palacky University, Slechtitelu 11, 783 71 Olomouc, Czech Republic

⁷Department of Chemistry and Molecular Biology, University of Gothenburg, Kemigården 4, SE-412 96 Gothenburg, Sweden

The development of artificial photosynthetic systems for converting solar energy and H₂O into solar fuels such as H₂ has attracted and still attracts enormous interest to lead the energy economy to a higher sustainability. The use of semiconductors in the Photo-Electro-Chemical (PEC) water splitting is the most promising approach in terms of scale-up technology to yield highly pure H₂.

In PEC water splitting, a semiconductor immersed in solution and coupled to a counter-electrode is illuminated by solar light. Light absorption by the semiconductor causes the formation of electron/hole pairs, which are separated and can drive two half-reactions thanks to the electrical field generated within the semiconductor at the Semi-Conductor/Liquid Junction (SCLJ). Quite often, this requires the help of an external applied potential (bias). For n-type semiconductors, the anodic reaction (that proceeds thanks to the transfer of holes to the electrolyte) occurs at the semiconductor's surface while the cathodic one is driven at the counter-electrode.

In the case of water splitting, the anodic process is the Oxygen Evolution Reaction (OER, here described in basic media):



That is a complicated reaction due to the need of exchange 4 electrons for each O₂ molecule. In a symmetric fashion, a p-type semiconductor can work as a photocathode, where the cathodic reaction (transfer of electrons to the electrolyte, i.e. water reduction to hydrogen) occurs while the anodic one occurs at the counter-electrode.

Semiconductors are usually characterized by sluggish OER kinetics thus limiting the overall system efficiency. To overcome this limitation, a suitable electrocatalyst can be deposited on the semiconductor surface. One of the most active materials is iridium oxide, whose catalytic cycle has been disclosed by us quite recently.

In a previous experiment at the ESRF (CH-4209) we carried out seminal experiments devoted to reach the most suitable experimental conditions for operando XAS experiment in photoelectrochemistry. For example, we studied the filling of the Ir 5d band when IrO_x is supported on an α-Fe₂O₃ nanostructured layer and under illumination with a 400 nm LED.¹ A similar system was investigated by the first pump & probe operando XAS experiment.²

The main issue in recording XAS spectra of photoelectrodes under operative condition is to guarantee a suitable acquisition strategy that allows to observe the quite small spectral changes due to the effect of visible light. The main winning strategies that we adopted are:

1) The acquisition of differential spectra: for each X-ray energy value the acquisition was performed both under LED light and in the dark. This minimizes possible systematic errors and ensures that for each energy value the absorption coefficient under light and dark conditions is measured under the same instrumental conditions and thus directly subtracted.

2) FEXRAV (fixed energy X-ray absorption spectroscopy): the X-ray energy is kept constant, at a value that corresponds to the highest contrast between the absorption coefficient of different standards phases. During the acquisition of the absorption coefficient, the electrode potential is varied at will. This hyphenated technique guarantees the joint acquisition of the electrochemical and the spectroscopic information in sync.

(i) The study of photocathodes

Here we studied Cu_2O and CuO p-type semiconductors (Cu K edge) as well as iron oxyhydroxides (Fe K edge) as possible overlayers. These materials promising performances have an added value thanks to the easiness of preparation and the wide absorption spectrum in the visible region. However, one of the drawbacks of both Cu-based photocathodes is their low stability that demands a deeper investigation for the understanding of the degradation mechanisms and to enhance their performance. In these experiments we compared electrodeposited Cu_2O with CuO (the latter prepared by annealing of CuI nanoparticles). Similar performances are accompanied by a higher stability of the second material: the analysis of XANES and FEXRAV results evidenced a partial reduction to Cu(I) under operative conditions. This generates a core-shell $\text{CuO/Cu}_2\text{O}$ system (Figure 1), in turn preventing the further reduction to metallic Cu .

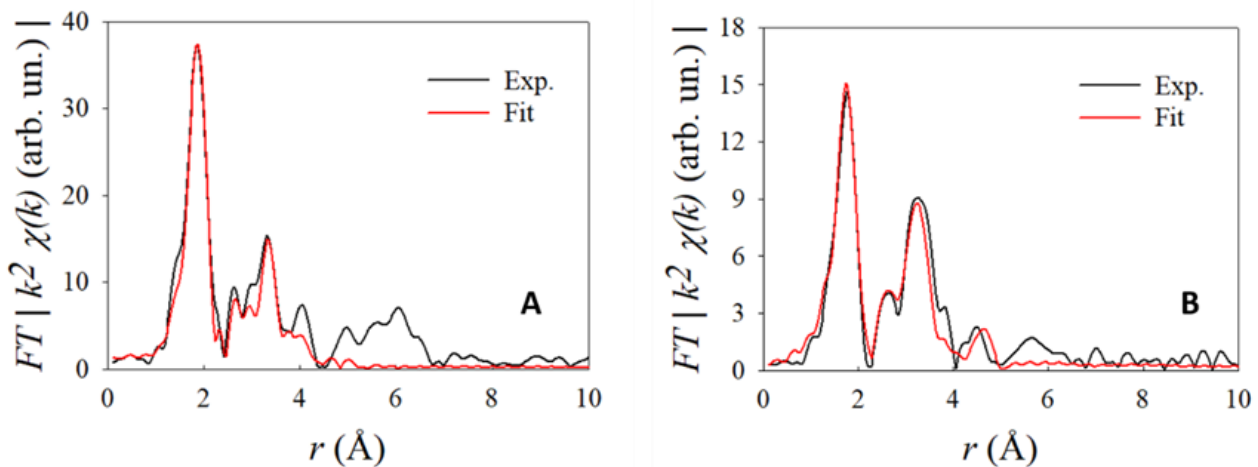


Fig. 1: Cu K-edge Fourier Transform of A) CuO electrode and B) CuO electrode kept at 0.3 V vs. RHE for 8 h upon irradiation at 400 nm. The black line represents the experimental data, and the red line is the fit. After 8 hours, the FT fit shows 30% CuO and 70% Cu_2O .

One experiment was devoted to study FeOOH that represents an interesting catalyst for the HER and, thanks to the easy and mild-conditions preparation method (electrodeposition from a Mohr's salt, that leads to a crystalline material), it is also a promising candidate as protective layer for the Cu-based one. This choice comes from the consideration that α - FeOOH (goethite) and γ - FeOOH (lepidocrocite) are commonly found on cathodes in industrial processes when steel is used as cathode for water reduction. We wanted to verify this mechanism when the material is deposited onto an inert support (i.e. in an electrochemical setup) or onto the photoanode. Analysis of the whole XAS spectrum (EXAFS+XANES) prompted us proposing a structure bearing a relation with that of green rust that is forming under hydrogen evolution. This phase is found independently on the phase of the initial electrode, either α - or γ - FeOOH .

Interestingly, during the electrochemical reoxidation, the original phase is restored, meaning that the reduced phase brings some memory of the structure of the pristine material.

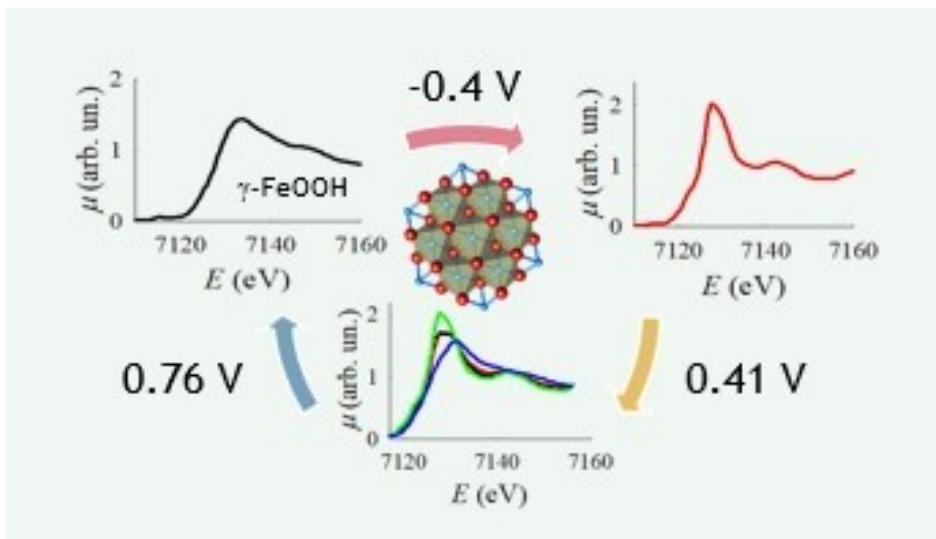


Fig. 2: Electrochemical behavior of γ -FeOOH. At -0.4 V the electrode is reduced and forms reduced green rust: the structure is shown. Upon re-oxidization the original phase (γ -FeOOH) is restored.

(ii) The study of photoanodes

In this case, two systems were considered, namely NiOOH/ α -Fe₂O₃ (Ni K edge) and WO₃ (W L_{III} edge). In both cases, the experimental results are at the basis of two publications under preparation.

The first system was taken into consideration after its high performances under visible light, low cost and to study the role of the NiOOH overlayer. In this case, the analysis of the Ni K edge XANES revealed the presence of Ni(IV) under illumination and with an applied bias, i.e. under oxygen evolution conditions. This evidence, coupled to complementary results from cyclic voltammetry and electrochemical impedance spectroscopy, allows us to better define the role of semiconductor overlayers and particularly the effect of the thickness.

The second system, WO₃, was selected as the optimal semiconductor to be studied by hard X-rays: this high performance material is based on a 5d element, thus allowing the study of the 2p → 5d excitation by means of the white line in the L_{III} XANES. In this case, changes in shape and intensity of the XANES peak evidence a partial occupancy of the t_{2g} band under illumination at open circuit. When a bias is applied, this effect is significantly reduced, likely because of the drain of photogenerated electrons towards the counter electrode. Interestingly, FEXRAV gave insights on the long-term dynamics of the process (in the orders of seconds) that have never been reported for an operando XAS experiment in photoelectrochemistry.

Publications: [ACS Appl. Mater. Interfaces 8 (2016) 21250, ACS Appl. Energy Mater. 1 (2018) 1716]

References

- (1) Minguzzi, A.; Naldoni, A.; Lugaresi, O.; Achilli, E.; D'Acapito, F.; Malara, F.; Locatelli, C.; Vertova, A.; Rondinini, S.; Ghigna, P. Phys. Chem. Chem. Phys. 2017, 19 (8), 5715.
- (2) Baran, T.; Fracchia, M.; Vertova, A.; Achilli, E.; Naldoni, A.; Malara, F.; Rossi, G.; Rondinini, S.; Ghigna, P.; Minguzzi, A.; D'Acapito, F. Electrochim. Acta 2016, 207, 16.

Correlation between atomic ordering and magnetic properties in binary magnetic alloys

S. Laureti¹, N. Safonova², A. Capobianchi¹, A. Puri³, E. Patrizi¹, F. D'Acapito³

¹nM2-lab, ISM-CNR, ²Institute of Physics, University of Augsburg, ³LISA - ESRF

Nowadays, the development of new advanced technologies in the field of information storage and electronic devices requires a great effort in improving the performance of magnetic materials that are at the basis of the device's functioning. Among the magnetic materials, the *3d-5d* chemically ordered binary alloys ($L1_0$, $L1_2$) are of significant interest due to the peculiar atomic arrangement within the crystallographic cell, which induces in the material, through the spin-orbit interaction, a high magnetocrystalline anisotropy [1].

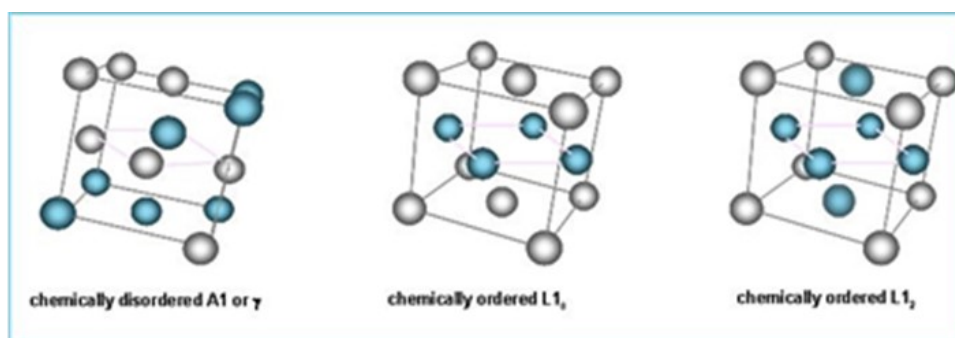


Fig. 1: Schematic representation of the crystallographic disordered and ordered structures

The BAG project aimed at investigating by X-ray Absorption Spectroscopy (XAS) the structural properties and the degree of chemical order within different magnetic alloys in form of thin films, powders and bilayers and to understand the influence of specific process conditions on the disordered-ordered transformation and, consequently, on the magnetic behaviour.

It is well known, for example, that the magnetic anisotropy can be varied by introducing a magnetic third element (Mn, Cr or Tb) to the FePt alloy, which is able to significantly affect not only the structural and chemical order but also the spin configuration (ferromagnetic or antiferromagnetic coupling among the magnetic elements) thus inducing a variation in the saturation magnetization. The effect of Tb content has been studied in series of $(\text{FePt})_{1-x}\text{Tb}_x$ thin films sputter deposited on MgO(100) substrates at 700°C. The Tb content x was varied in the range 5 – 28 at.% by altering the Tb deposition rate while keeping the Fe and Pt rates constant. EXAFS spectra at the Pt-L_{III} edge was collected on samples with different Tb content and a substitutional model was considered, aimed to verify if Tb atom substitutes the Fe or Pt atoms in the $L1_0$ FePt lattice, according to the method applied for the FePt:Cu system in Ref. 2.

For all samples, the fit excluded the presence of a Tb scattering element in the first neighbours shell around Pt. As a consequence, a pure FePt model has been considered to fit the FT data in the range $R=1.5-3.2 \text{ \AA}$ and $k = 2-10 \text{ \AA}^{-1}$. Although the Tb does not enter directly into the FePt lattice, its effect on the $L1_0$ structure has been evidenced by the contraction of all the distances and, more precisely, on a deformation of the tetragonal structure toward a cubic symmetry, typical of the chemically disordered structure (A1 FePt), whose low magnetocrystalline anisotropy is confirmed by the room temperature hysteresis loops (Fig. 2).

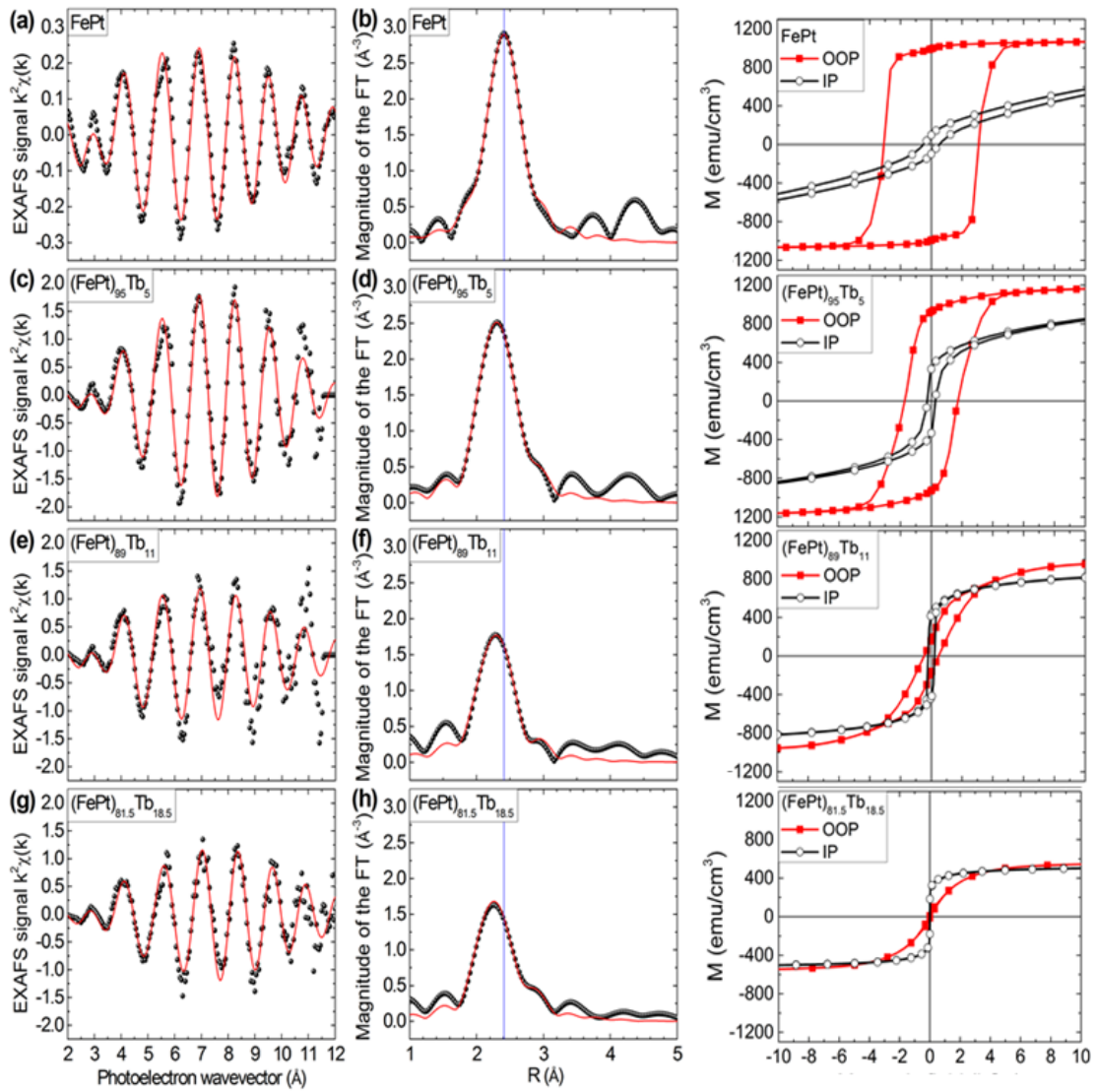


Fig. 2: EXAFS signals (left column) at the Pt-L III edge and the relative Fourier Transform (right column) of the reference; out-of-plane (OOP) and in-plane (IP) M-H hysteresis loops measured at 300 K

The high process temperature used to induce the transformation from the disordered A1 to the highly ordered L1₀ FePt alloy in thin films represents a noticeable disadvantage in nanoparticles, due to the particle coalescence phenomena with the consequent increase of the particle size, size dispersion, and reduction of the magnetic anisotropy. Recently, a new chemical strategy has been reported, aimed at obtaining the direct synthesis of L1₀ FePt alloy nanoparticles starting from a polycrystalline molecular compound, the iron (II) chloroplatinate hexahydrate (FePtCl₆ · 6H₂O), in which Fe and Pt atoms are arranged on alternating planes (fig. 3) like in the fct FePt structure [3, 4]

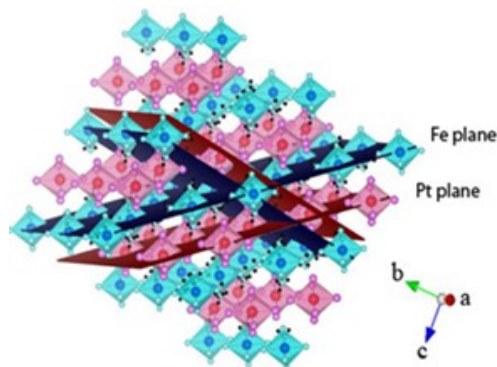


Fig. 3: FePtCl₆ · 6H₂O structure

The XAS experiment carried on at LISA beamline consisted in two parts:

- 1) ex-situ analysis: the local structural evolution during the treatment has been studied by EXAFS carried out on the powder samples prepared in the home laboratory at the Fe-K and Pt-L_{III} edges in transmission mode, in order to obtain a description of the local environment around these metals in the initial crystal, during the treatment (i.e. in samples annealed at intermediate temperature) and in the final product.
- 2) in-situ analysis: samples of FePtCl₆ · 6H₂O crystalline film has been put into a heating cell designed for in-situ X-ray absorption experiments at high temperature and under a reactive atmosphere (fig. 3).



Fig. 4: Microtomo Furnace
[\[http://www.esrf.eu/home/UsersAndScience/Experiments/Scilnfra/SampleEnvironment/high-temperature/microtomo-furnace.html\]](http://www.esrf.eu/home/UsersAndScience/Experiments/Scilnfra/SampleEnvironment/high-temperature/microtomo-furnace.html).

Once verified the reproducibility of the heating process into the LISA furnace, the annealing has been performed by heating the powder sample at 400 °C with a rate of 5 °C/min, under H₂/Ar reductive atmosphere. Quick-XANES spectra have been collected at the Fe-K_α and Pt-L_{III} edge in transmission mode, during two separated processes to follow the chemical/structural evolution around the two elements during the treatment. Spectra of 4s/each have been collected at a rate of 3 spectra/minute every 10 °C of the heating process. The same apparatus has been also used to carry out static EXAFS experiments in stationary temperature conditions (i.e. EXAFS spectra acquired at defined temperatures of the heating treatment).

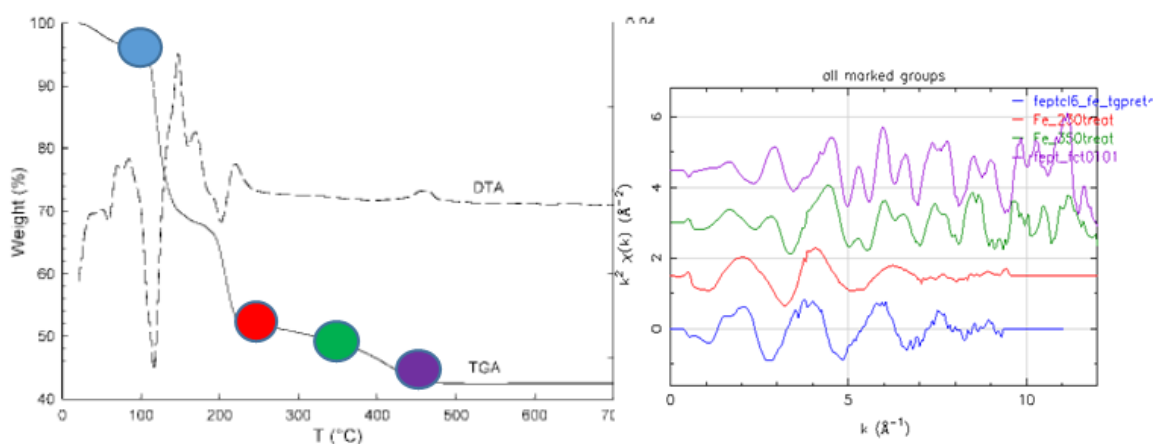


Fig. 5: TGA-DTA of FePtCl₆ · 6H₂O under flux of 95% Ar and 5% H₂ (left); comparison between EXAFS signals at the Pt-L_{III} edge obtained at different temperatures during the treatment.

The study revealed a high degree of chemical ordering obtained by the proposed method and allowed the validation of the precursor strategy since the presence of a peculiar ordered arrangement between Pt and Fe planes can be deduced from the analysis of the EXAFS spectra already in the intermediate structure, i.e. before the end of the chemical reduction.

Publication: [Phys. Rev. B (2019), Submitted.]

References:

- [1] A. Cebollada et al., Magnetic nanostructures, H. Nalwa (Ed), American Scientific Publishers, 2002, ch. 3 (2002) 93
- [2] Laureti, et al., J. Appl. Cryst. 47 (2014) 1722
- [3] A. Capobianchi, et al, Chemistry of Materials 21 (2009) 2007;
- [4] A. Capobianchi et al. Z. Kristallogr. 224 (2009) 384–388

XRF and XANES spectra for studies of cryospheric science at the LISA beamline

G. Baccolo^{1,2}, C. Baroni^{3,4}, G. Cibin⁵, B. Delmonte¹, Zhiheng Du⁶, Shiwei Liu⁶, S. Macis^{7,8}, V. Maggi^{1,2}, A. Marcelli^{7,9},
A. Puri¹⁰, M.C. Salvatore^{3,4}, Wei Xu¹¹

¹Environmental and Earth Sciences Department, University of Milano-Bicocca, Italy; ²INFN, Milano-Bicocca Section, Milano, Italy; ³Earth Sciences Department, University of Pisa, Italy; ⁴Istituto di Geoscienze e Georisorse, Pisa, Italy; ⁵Diamond Light Source, Didcot, UK; ⁶State Key Laboratory of Cryospheric Science, Northwest Institute of Eco-Environment and Resources, Chinese Academy of Science, Lanzhou, China; ⁷INFN, Laboratori Nazionali di Frascati, Italy; ⁸Università di Tor Vergata, Roma, Italy; ⁹Rome International Center for Materials Science Superstripes, Italy; ¹⁰CNR-IOM-OGG, ESRF, LISA CRG, Grenoble, France; ¹¹Beijing Synchrotron Radiation Facility, Institute of High Energy Physics, Chinese Academy of Sciences, Beijing, China

In the last two years (2017-2018) a fruitful Chinese-Italian collaboration was established in the field of polar and cryospheric sciences in the framework of the proposal 08-01-1031. Here we summarize some of the preliminary results about the activities that the present collaboration pursued at BM08 - LISA, the Italian beamline for X-ray Absorption Spectroscopy at ESRF. The core of our research was focused on the geochemical characterization of samples consisting in atmospheric mineral dust entrapped in snow and ice, and in samples collected from dust potential source areas. Polar and high-altitude regions were taken into account: Antarctica, the Tibetan Plateau, the Svalbard archipelago and other Arctic locations. The importance of studying the atmospheric dust cycle in such fragile environments is multiple [Bullard et al., 2016]. Considering different spatial and temporal perspectives, with these unique spectroscopic data it is possible to investigate many peculiar processes.

As an example, considering the Tibetan Plateau, it is possible to better understand the role played by the atmospheric dust that is deposited on the glaciers of this region. It is known that specific mineral fractions, as iron oxides, are extremely sensitive to solar light adsorption and can thus influence the radiative budget of glaciers and the ice melting process [Cong et al., 2018].

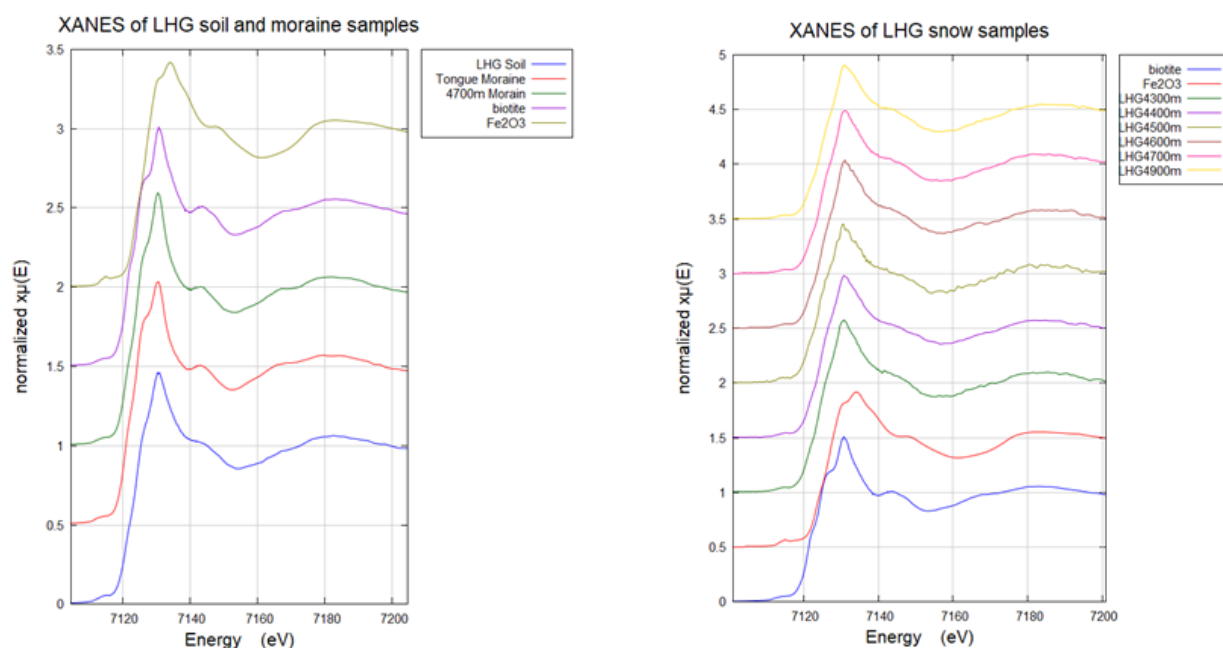


Fig. 1 XANES spectra at the Fe K-edge of soil and moraine samples collected in the Tibetan Plateau region (left) and from mineral dust extracted from snow samples (right).

Other important topics concern the human impacts on the geochemical properties of snow and particulate matter deposited on the glaciers [Li et al., 2018] and the geochemical transformations that affect aerosols and dust during the atmospheric transport. Atmospheric mineral dust is extremely important in the Antarctic also, since the amount and the composition of dust that is found in ice core samples is strictly related to the climatic conditions [Lambert et al., 2008]. Studying the dust records obtained from Antarctic ice cores it is possible to obtain important pieces of information concerning the climatic and environmental conditions of the dust source areas [Maher et al., 2010]. In this context a challenging task is the recognition of the dust sources in the different climatic periods. Their identification allows for a better understanding of past atmospheric trajectories and of past environmental conditions, since the emission, transport and deposition of mineral dust are all related to them.

In 2018 we performed three experimental runs at LISA and about 100 samples were analysed, they consisted in aerosol extracted from Arctic and Antarctic snow and ice, mineral particulate matter collected from Antarctic dust source areas, Chinese loess samples and cryoconite from the Italian Alps. For each sample we collected XRF and XAS spectra. XRF spectra were acquired to constrain the rough composition of the samples. XAS analyses were focused on iron. This element is among the most important when considering biogeochemistry. We decided to pay attention to it because of its importance related to optical and energetic processes, but also because it is an essential element for many ecosystems and atmosphere can be the only source for iron, as it commonly happens in oceanic open waters [Jickells et al., 2005] or polar and high-altitude environments [Hawkings et al., 2018; Du et al., 2019]. Thanks to XAS spectroscopy it was possible to acquire Fe K-edge spectra and investigate the mineralogical and speciation features of this element [Cibin et al., 2008; Marcelli et al., 2012&2012a]. Some examples are presented in Figure 1, where spectra concerning Fe K-edge of samples from Laohugou No.12 glacier (Tibetan Plateau, Figure 1 right) are compared to samples collected from the peri-glacial environment to verify if any correlation between them exists. This step was specifically carried out through the linear fit combination (LCF). All samples (glacial and peri-glacial environment) could be reproduced by a mixture composed of Fe_2O_3 , Fe_3O_4 , biotite and ferrous oxalate dihydrate (FOD). A preliminary analysis of the data revealed that snow samples are affected by a significant altitude effect could be detected for snow. The proportion of Fe_2O_3 in snow decreases gradually at increasing altitude, while FOD shows an opposite behaviour. Further efforts will be needed to understand the correlation between potential source areas and our samples.

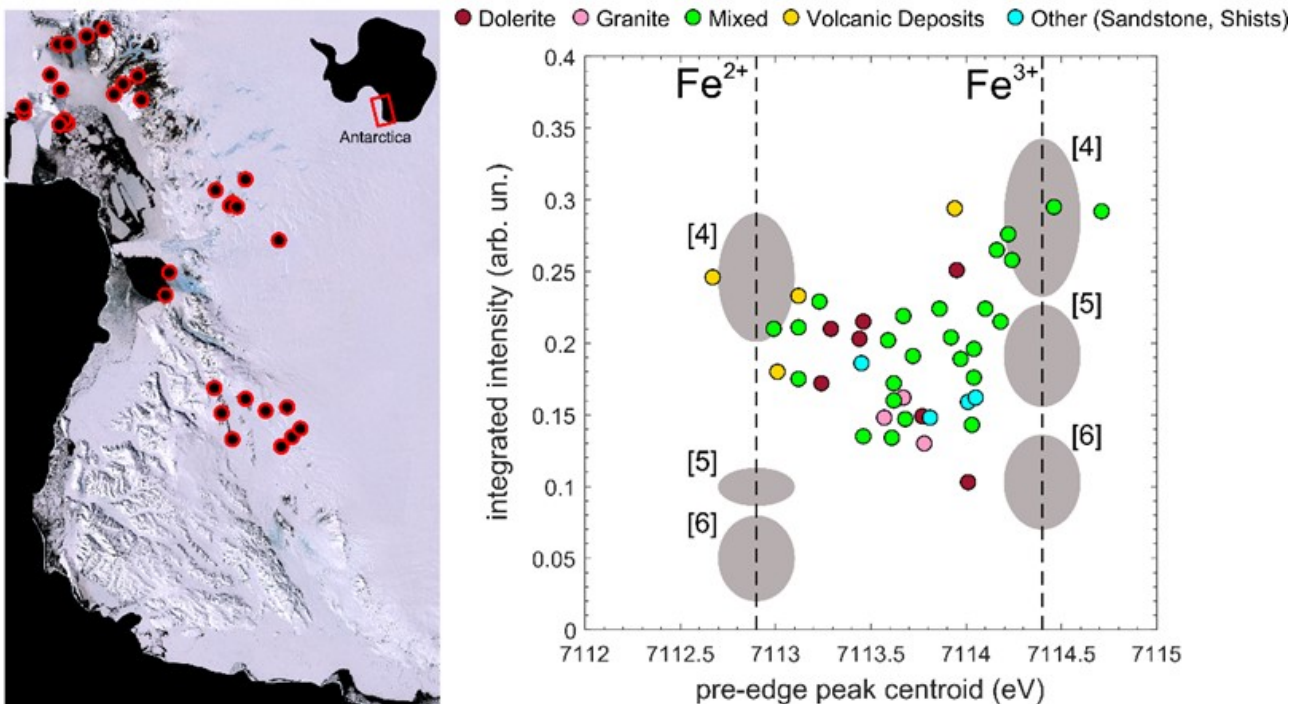


Fig. 2: On the left the map showing the location of the Antarctic samples from potential dust source areas that were analysed through XAS spectroscopy at LISA. Samples were collected from ice-free regolith outcrops, raised beaches, natural aeolian traps and glacial drift. On the right preliminary XANES results, data are presented following the scheme proposed by Wilke et al. (2001) where domains related to iron oxidation and coordination are highlighted

In Figure 2 preliminary results concerning XANES analysis of the samples collected from Antarctic potential dust source areas are presented. We adopted the scheme proposed by Wilke et al. (2001) to highlight the relative contribution of Fe²⁺ and Fe³⁺ and their coordination state. It is possible to see that despite the limited set of samples, some lithologies are well separated, for example volcanic deposits with a single exception, present a higher ferrous content, in accordance to the abundance of Fe²⁺ that was recently found in volcanic events recorded in ice cores [Bugay et al., 2019]. A full comparison between data retrieved from an ice core drilled in the same Antarctic sector [Maggi et al., 2018] and these new data is in progress, in order to understand the role played by local Antarctic dust sources in the Antarctic atmospheric dust cycle.

Several XAS spectra have been collected mainly at the iron K-edge and confirm the variability of mineralogy on snow, ice, aerosols, loess and dust samples with different provenances. Substantial improvements in the detection limits, reliability and detection efficiency have been demonstrated thanks to the installation and commissioning of the new monochromator with Si (111) crystals and the new control system. Additional and relevant improvements have been experienced also with the new four elements detector. Three manuscripts have been already published and others are in preparation.

Publications:

- [1. Baccolo, G.; Cibin, G.; Delmonte, B.; Hampai, D.; Marcelli, A.; Di Stefano, E.; Macis, S.; Maggi, V. The Contribution of Synchrotron Light for the Characterization of Atmospheric Mineral Dust in Deep Ice Cores: Preliminary Results from the Talos Dome Ice Core (East Antarctica). *Condens. Matter* 2018, 3, 25]
- [2. Maggi, V.; Baccolo, G.; Cibin, G.; Delmonte, B.; Hampai, D.; Marcelli, A. XANES Iron Geochemistry in the Mineral Dust of the Talos Dome Ice Core (Antarctica) and the Southern Hemisphere Potential Source Areas. *Condens. Matter* 2018, 3, 45]
- [3. Liu, S.; Xiao, C.; Du, Z.; Marcelli, A.; Cibin, G.; Baccolo, G.; Zhu, Y.; Puri, A.; Maggi, V.; Xu, W. Iron Speciation in Insoluble Dust from High-Latitude Snow: An X-ray Absorption Spectroscopy Study. *Condens. Matter* 2018, 3, 47]
- [4. Oral contributions presented at the Italian/Chinese Bilateral Workshop Aerosols in Snow and ice: markers of environmental pollution and climatic changes: European and Asian perspectives (Rome, September 7-8, 2017); <https://www.superstripes.net/science/aerosols-in-snow-and-ice.pdf>]

References:

- [Bullard J.E., et al. "High latitude dust in the Earth system" *Reviews of Geophysics* **54**:447-485 (2016)]
- [Bugay F., et al., "Fe²⁺ in ice cores as a new potential proxy to detect past volcanic eruptions" *Science of the Total Environment* **654**:1110-117 (2019)]
- [Cibin, G., et al., "First combined total reflection X-ray fluorescence and grazing incidence X-ray absorption spectroscopy characterization of aeolian dust archived in Antarctica and Alpine deep ice cores" *Spectrochimica Acta Part B* **63**: 1503–1510 (2008)]
- [Cong Z., et al. "Iron oxides in the cryoconite of glaciers on the Tibetan Plateau: abundance, speciation and implications" *Cryosphere* **12**:3177-3186 (2018)]
- [Du Z., et al., "Iron record associated with sandstorms in a central Asian shallow ice core spanning 1956-2004" *Atmospheric Environment in press* (2019)]
- [Hawkings J.R., et al., "Biolabile ferrous iron bearing nanoparticles in glacial sediments" *Earth and Planetary Science Letters* **493**:92-101 (2018)]
- [Jickells T.D., et al., "Global iron connections between desert dust, ocean biogeochemistry and climate" *Science* **308**:67-71 (2005)]
- [Lambert F., et al., "Dust-climate couplings over the past 800,000 years from the EPICA Dome C ice core" *Nature* **452**:616-619 (2008)]
- [Li Y., et al., "Signals of pollution revealed by trace elements in recent snow from mountain glaciers at the Qinghai–Tibetan plateau" *Chemosphere* **200**:523-531 (2018)]
- [Maggi V., et al., "XANES Iron Geochemistry in the Mineral Dust of the Talos Dome Ice Core (Antarctica) and the Southern Hemisphere Potential Source Areas" *Condensed Matter* **3**:45 (2018)]
- [Maher B.A., et al., "Global connections between aeolian dust, climate and ocean biogeochemistry at the present day and at the last glacial maximum" *Earth Science Reviews* **99**:61-97 (2010)]
- [Marcelli, A., et al., "XRF-XANES characterization of deep ice core insoluble dust in the ppb range" *J. Anal. At. Spectrom.* **27**: 33-37 (2012)]
- [Marcelli, A., et al., "Local vs. global climate change - investigation of dust from deep ice cores" *Spectroscopy Europe* **24**: 12-17 (2012a)]
- [Wilke M., et al., "Oxidation state and coordination of Fe in minerals: An Fe K-XANES spectroscopic study" *American Mineralogist* **86**: 714-730 (2001)]

1. Baekelant W., Aghakhani S., Coutiño-Gonzalez E., Kennes K., Grandjean D., Van der Auweraer M., Lievens P., Roeffaers M.B.J., Hofkens J., Steele J.A. - Shaping the optical properties of silver clusters inside zeolite A via Guest–Host–Guest Interactions, *Journal of Physical Chemistry Letters* 9, 5344-5350 (2018)
2. Fracasso G., Ghigna P., Nodari L., Agnoli S., Badocco D., Pastore P., Nicolato E., Marzola P., Mihajlovic D., Markovic M., Colic M., Amendola V. - Nanoaggregates of iron poly-oxo-clusters obtained by laser ablation in aqueous solution of phosphonates, *Journal of Colloid and Interface Science* 522, 208-216 (2018)
3. Fracchia M., Visibile A., Ahlberg E., Vertova A., Minguzzi A., Ghigna P., Rondinini S. - α - and γ -FeOOH: Stability, reversibility, and nature of the active phase under hydrogen evolution, *ACS Applied Energy Materials* 1, 1716-1725 (2018)
4. Giuli G., Eisenmann T., Bresser D., Trapananti A., Asenbauer J., Mueller F., Passerini S. - Structural and electrochemical characterization of Zn_{1-x}Fe_xO—effect of aliovalent doping on the Li⁺ storage mechanism, *Materials* 11, 49-1-49-13 (2018)
5. Grandjean D., Coutiño-Gonzalez E., Cuong N.T., Fron E., Baekelant W., Aghakhani S., Schlexer P., d'Acapito F., Banerjee D., Roeffaers M.B.J., Nguyen M.T., Hofkens J., Lievens P. - Origin of the bright photoluminescence of few-atom silver clusters confined in LTA zeolites, *Science* 361, 686-690 (2018).
6. Jacyna I., Klinger D., Pelka J.B., Minikayev R., Dluzewski P., Dynowska E., Jakubowski M., Klepka M.T., Zymierska D., Bartnik A., Kurant Z., Wolska A., Wawro A., Sveklo I., Plaisier J.R., Eichert D., Brigidi F., Makhotkin I., Maziewski A., Sobierajski R. - Study of ultrathin Pt/Co/Pt trilayers modified by nanosecond XUV pulses from laser-driven plasma source, *Journal of Alloys and Compounds* 763, 899-908 (2018)
7. Jehle F., Fratzl P., Harrington M.J. - Metal-tunable self-assembly of hierarchical structure in mussel-inspired peptide films, *ACS Nano* 12, 2160-2168 (2018)
8. Jouve A., Nagy G., Somodi F., Tiozzo C., Villa A., Balerna A., Beck A., Evangelisti C., Prati L. - Gold-silver catalysts: Effect of catalyst structure on the selectivity of glycerol oxidation, *Journal of Catalysis* 368, 324-335 (2018)
9. Liao T.W., Yadav A., Hu K.J., van der Tol J., Cosentino S., d'Acapito F., Palmer R.E., Leonard C., Ferrando R., Grandjean D., Lievens P. - Unravelling the nucleation mechanism of bimetallic nanoparticles with composition-tunable core–shell arrangement, *Nanoscale* 10, 6684-6694 (2018)
10. Maurizio C., Edla R., Michieli N., Orlandi M., Trapananti A., Mattei G., Miotello A. - Two-step growth mechanism of supported Co₃O₄-based sea-urchin like hierarchical nanostructures, *Applied Surface Science* 439, 876-882 (2018)
11. Maurizio C., Michieli N., Kalinic B., Mattarello V., Bello V., Wilhelm F., Ollefs K., Mattei G. - Local structure and X-ray magnetic circular dichroism of Au in Au-Co nanoalloys, *Applied Surface Science* 433, 596-601 (2018)
12. Moretti A., Giuli G., Trapananti A., Passerini S. - Electrochemical and structural investigation of transition metal doped V₂O₅ sono-aerogel cathodes for lithium metal batteries, *Solid State Ionics* 319, 46-52 (2018)

13. Ottini R., Tealdi C., Tomasi C., Tredici I.G., Soffientini A., Burriel R., Palacios E., Castro M., Anselmi-Tamburini U., Ghigna P., Spinolo G. - Local environments and transport properties of heavily doped strontium barium niobates Sr_{0.5}Ba_{0.5}Nb₂O₆, *Journal of Solid State Chemistry* 258, 99-107 (2018)
14. Pethes I., Chahal R., Nazabal V., Prestipino C., Michalik S., Darpentigny J., Jóvári P. - Chemical order in Ge-Ga-Sb-Se glasses, *Journal of Non-Crystalline Solids* 484, 49-56 (2018)
15. Popov V.V., Menushenkov A.P., Gaynanov B.R., Ivanov A.A., d'Acapito F., Puri A., Shchetinin I.V., Zheleznyi M.V., Berdnikova M.M., Pisarev A.A., Yastrebtsev A.A., Tsarenko N.A., Arzhatkina L.A., Horozova O.D., Rachenok I.G., Ponkratov K.V. - Formation and evolution of crystal and local structures in nanostructured Ln₂Ti₂O₇ (Ln =Gd–Dy), *Journal of Alloys and Compounds* 746, 377-390 (2018)
16. Quaretti M., Porchia M., Tisato F., Trapananti A., Aquilanti G., Damjanović M., Marchiò L., Giorgetti M., Tegoni M. Thermodynamic stability and structure in aqueous solution of the [Cu(PTA)₄]⁺ complex (PTA = aminophosphine- \square 1,3,5-triaza-7-phosphaadamantane) - *Journal of Inorganic Biochemistry* 188, 50-61 (2018)
17. Rizzato S., Moret M., Beghi F., Lo Presti L. - Crystallization and structural properties of a family of isotopological 3D-networks: The case of a 4,4'-bipy ligand–M₂⁺ triflate system, *CrystEngComm* 20, 3784-3795 (2018)
18. Schnohr C.S., Eckner S., Schöppe P., Haubold E., d'Acapito F., Greiner D., Kaufmann C.A. - Reversible correlation between subnanoscale structure and Cu content in co-evaporated Cu(In,Ga)Se₂ thin films, *Acta Materialia* 153, 8-14 (2018)
19. Stellato F., Calandra M., d'Acapito F., De Santis E., La Penna G., Rossi G., Morante S. - Multi-scale theoretical approach to X-ray absorption spectra in disordered systems: an application to the study of Zn(II) in water, *Physical Chemistry - Chemical Physics* 20, 24775-24782 (2018)
20. Terashima K., Paris E., Simonelli L., Salas-Colera E., Puri A., Wakita T., Yamada Y., Nakano S., Idei H., Kudo K., Nohara M., Muraoka Y., Mizokawa T., Yokoya T., Saini N.L. - Temperature-dependent local structure and superconductivity of BaPd₂As₂ and SrPd₂As₂, *Physical Review B* 98, 94525-1-49525-5 (2018)
21. Veber A., Cicconi M.R., Puri A., de Ligny D. - Optical properties and bismuth redox in Bi-doped high-silica Al–Si glasses, *Journal of Physical Chemistry C* 122, 19777-19792 (2018)
22. Martinelli, A., Lepore, G. O., Bernardini, F., Giaccherini, A., & Di Benedetto, F.- The puzzling structure of Cu₅FeS₄ (bornite) at low temperature, *Acta Crystallographica Section B: Structural Science, Crystal Engineering and Materials* 74.5 (2018).
23. Baekelant, W.; Aghakhani, S.; Coutino-Gonzalez, E.; Grandjean, D.; Kennes, K.; Jonckheere, D.; Fron, E.; d'Acapito, F.; Longo, A.; Lievens, P. ; Roeffaers, M.B.J.; Hofkens, J., Confinement of Highly Luminescent Lead Clusters in Zeolite A, *JOURNAL OF PHYSICAL CHEMISTRY C*122 (2018) 13953-13961.
24. Liu, S.; Xiao, C.; Du, Z.; Marcelli, A.; Cibirin, G.; Baccolo, G.; Zhu, Y.; Puri, A.; Maggi, V.; Xu, W. Iron Speciation in Insoluble Dust from High-Latitude Snow: An X-ray Absorption Spectroscopy Study. *Condensed Matter*, 3 (2018) 47.

Beamline responsible: **Francesco d'Acapito**
dacapito@esrf.fr
+33 4 7688 2426 , +33 6 8936 4302

Beamline scientists: **Alessandro Puri**
puri@esrf.fr
+33 4 7688 2859

Giovanni Orazio Lepore
lepore@esrf.fr
+33 4 7688 2530

Local Contact: +33 6 8838 6994
Beamline: +33 4 7688 2085
Laboratory: +33 4 7688 2743
Skype: gilda_beamline

Administration: **Fabrizio La Manna**
lamanna@esrf.fr
+33 4 7688 2962

Web page: <http://www.esrf.eu/UsersAndScience/Experiments/CRG/BM08/>

Forthcoming proposals submission deadlines

Due to the construction of the EBS source there will be no call for proposals in 2019.

7. Contributors to this issue

F. d'Acapito, A. Puri, G. O. Lepore (CNR-IOM, Grenoble), R. de Donatis (CNR-SPIN, Genova), M. R. Cicconi (IPGP, Paris), S. E. Ali (Suez Canal Univ.), A. Fantin (TU, Berlin), D. Grandjean (KU Leuven), S. Laureti (CNR-ISM, Montelibretti), A. Marcelli (INFN-LNF, Frascati), A. Martinelli (CNR-SPIN, Genova), A. Menushenkov (MEPhI, Moscow), A. Minguzzi (Univ. Statale, Milano).

Activity report
of the Italian CRG
beamline at the European
Synchrotron Radiation
Facility (ESRF)

LISA
Annual Report
2018